# A comparison of bistatic scattering from two geologically distinct abyssal hills

Chin Swee Chia[a] and Nicholas C. Makris[b]
*Massachusetts Institute of Technology, Cambridge, Massachusetts 02139*

Laurie T. Fialkowski
*Naval Research Laboratory, Washington, D.C. 20375*

(Received 22 September; revised 14 June 2000; accepted 16 June 2000)

The bistatic scattering characteristics of two geologically distinct abyssal hills located on the western flank of the Mid-Atlantic Ridge, known as B′ and C′, are experimentally compared using data acquired with low-frequency towed-array systems at $\frac{1}{2}$ convergence zone (~33 km) stand-off. The comparison is significant because the abyssal hills span the two classes of elevated seafloor crust that cover the Mid-Atlantic Ridge. The highly lineated B′ feature is representative of abyssal hills composed of outside corner crust, the most commonly occurring category, whereas the domed C′ promontory is representative of the rougher, low-aspect-ratio abyssal hills composed of inside corner crust. The latter are less common and usually restricted to segment valley margins. The mean biazimuthal scattering distributions of the two abyssal hills each exhibit Lambertian behavior with comparable albedos, suggesting that the distinction between abyssal hills composed of differing crust is not significant in modeling long-range reverberation. The adverse effect of using bathymetry that undersamples seafloor projected area in scattering strength analysis is also quantified with data from the B′ ridge. Specifically, the use of undersampled bathymetry can lead to significant overestimates in the strength of seafloor scattering. © *2000 Acoustical Society of America.* [S0001-4966(00)04410-6]

PACS numbers: 43.30.Hw, 43.30.Gv [DLB]

## I. INTRODUCTION

In this paper, a comparison is made of *bistatic* scattering from two geologically distinct abyssal hills located along a segment valley on the western flank of the Mid-Atlantic Ridge (MAR). This analysis is based on acoustic data acquired by low-frequency towed-array systems at $\frac{1}{2}$ convergence zone (CZ) (~33 km) stand-off during the Main Acoustics Experiment (MAE) of the Acoustic Reverberation Special Research Program (ARSRP) in July 1993.[1–4] A detailed analysis of bistatic scattering from one of these abyssal hills, named B′, has previously been presented in Ref. 3. The goal of this paper is to present a similar analysis for the second ridge, C′, for comparative purposes. The comparison is significant because the B′ and C′ abyssal hills span the two classes of elevated seafloor crust that cover the MAR. An acoustic analysis of these two prominent bathymetric features should then lead to a better understanding of the long-range, bistatic scattering properties of bathymetric highs throughout the MAR.

The B′ abyssal hill is composed of *outside corner* (OC) crust, whereas the C′ promontory is composed of *inside corner* (IC) crust.[5] This geological distinction has already helped to clarify measured differences in the spatial characteristics of *monostatic* reverberation from these two features.[4] The lineated B′ feature, by its high aspect ratio, is representative of abyssal hills composed of OC crust. The numerous steep escarpments that run along the major axis of OC abyssal hills, and B′ in particular, return echoes that faithfully image the lineated scarp morphology.[3,4] The domed C′ promontory is representative of the rougher, low-aspect-ratio abyssal hills composed of IC crust. Long-range acoustic images of C′ again faithfully image steep slopes on C′, but these show more amorphous, nonlinear structure.[4] Abyssal hills of OC crust occur more commonly, while those of IC crust are usually restricted to segment valley margins. Geologically, ''IC crust forms on the side of the spreading axis next to an active discontinuity and is characterized by anomalously shallow bathymetry, thinned crust and/or mantle exposures, irregular large-throw normal faults, and a paucity of volcanic morphological features. OC crust is formed on the opposite side of the spreading axis next to the inactive trace of the discontinuity; it has more normal depth and crustal thickness, regular fault patterns, and more common volcanic features.'' [5]

In a previous analysis of ARSRP data,[3] high-resolution bistatic reverberation images of B′ were generated from $\frac{1}{2}$ CZ stand-off. These measured images were compared with the modeled images, generated from 5-m resolution bathymetry data, to show that steep scarps on B′ return the strongest echoes because they project the largest surface areas along the acoustic path from source to scattering patch to receiver. Both measured and modeled images also show that prominent echo returns deterministically image the scarp morphology when the cross-range resolution of the towed-array system runs along the scarp axis. Although small-scale features along the scarp, such as canyons and gullies (~100–200-m scale), are theoretically resolvable in range by the towed-

[a]Current address: DSO National Laboratories, 20 Science Park Drive, S118230, Singapore.
[b]Electronic mail: makris@mit.edu

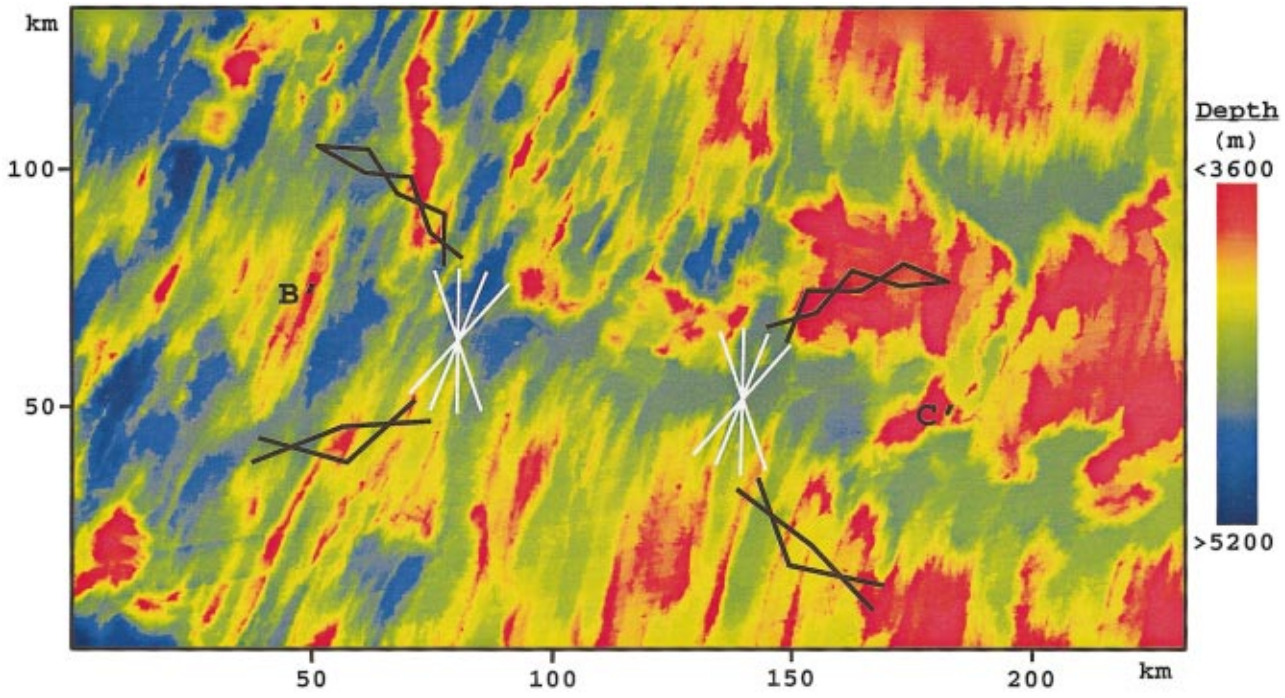


FIG. 1. Bistatic tow-ship tracks overlain on the 200-m resolution bathymetry data of the experimental area, extracted from Ref. 4. The B′ and C′ ridges are two prominent seafloor features at opposite ends of the segment valley that runs roughly east–west across the experimental area. White tracks denote the monostatic positions of RV CORY CHOUEST that trace the Easternstar and Westernstar, while the black tracks indicate the bistatic positions of RV ALLIANCE along the semicircular arcs about B′ and C′.

array system at some bistatic angles, statistical fluctuations due to signal-dependent noise present in the actual data prevent the system from resolving these features. This leads to the conclusion that signal-dependent noise, known as speckle, is one of the primary factors limiting the towed-array system's resolving power in imaging the seafloor geomorphology.[3,4,6]

In the same study, the biazimuthal scattering distribution functions[3] of the two major scarps on B′ were estimated using 5-m resolution bathymetry data. The mean strengths of the biazimuthal scattering distributions over the two scarps were shown to be identical and equal to the constant of $-17$ dB $\pm$ 8 dB. This lead to the hypothesis that long-range reverberation from prominent geomorphologic features of the world's Mid-Ocean Ridges may be adequately modeled as Lambertian with albedo $\pi/10$[1.7].

To further test this hypothesis, a similar study has been carried out to measure the biazimuthal scattering distribution function of a major scarp on the C′ abyssal hill. Since 5-m resolution bathymetry is unavailable at C′, the analysis is carried out with lower-resolution hydrosweep bathymetry data sampled at 200-m intervals.[7] To help control the comparison with C′ results, and quantify the potentially adverse effects of using undersampled bathymetry data in scattering strength estimation, the biazimuthal scattering distribution function for the B′ scarps are recomputed using the lower-resolution hydrosweep data. While a number of investigators have analyzed monostatic reverberation from B′[3,4,8,9] and bistatic reverberation from B′,[3,4] this is the first study[10] to analyze bistatic reverberation from C′.

## II. BISTATIC EXPERIMENTAL DESIGN AND GEOMORPHOLOGY OF THE TWO OCEAN RIDGES

The experiments took place within a subsection of the ONR Natural Laboratory spanning 25.5° to 27.5° North latitude and 45° to 49° West longitude along the western flank of the MAR.[1–5] Nine experiments, referred to as *runs* in the ARSRP community, were conducted. Bistatic scattering was measured at $\frac{1}{2}$ CZ stand-off from site B′ in runs 5a and 5b and from C′ in runs 3 and 8. The B′ and C′ abyssal hills are separated by a segment valley of roughly 2 CZ length which enabled a set of experiments at $\frac{1}{2}$ and 1 $\frac{1}{2}$ CZ to be conducted about each feature with extreme efficiency.[2,4,11] These experiments are therefore referred to as the B′–C′ *corridor* experiments, which comprised roughly 90% of the Main Acoustics Experiment.[1–4,11]

The experiments were conducted using two research vessels (RVs), the CORY CHOUEST and ALLIANCE.[12] Their bistatic tow-ship tracks are overlain on the local bathymetry in Fig. 1. During each run, CORY and ALLIANCE began at the edges of the star-shaped tracks with slow cruising speeds of 3.0–4.5 knots. While the CORY traced its straight-line path in the central star, the RV ALLIANCE zigzagged along semicircular arcs about B′ and C′. To maximize the sonar cross-range resolution at B′ and C′, the towed-array's broadside beam was directed towards each target abyssal hill, while the ships' radiated noise was restricted to the lowest-resolution endfire beams to minimize mutual noise interference.

It has been shown[3,4,13] that significant variations in reverberation can occur for small changes in measurement position due to bathymetry-induced variations in transmission loss (TL). The star-shaped ship tracks avoid the problem of

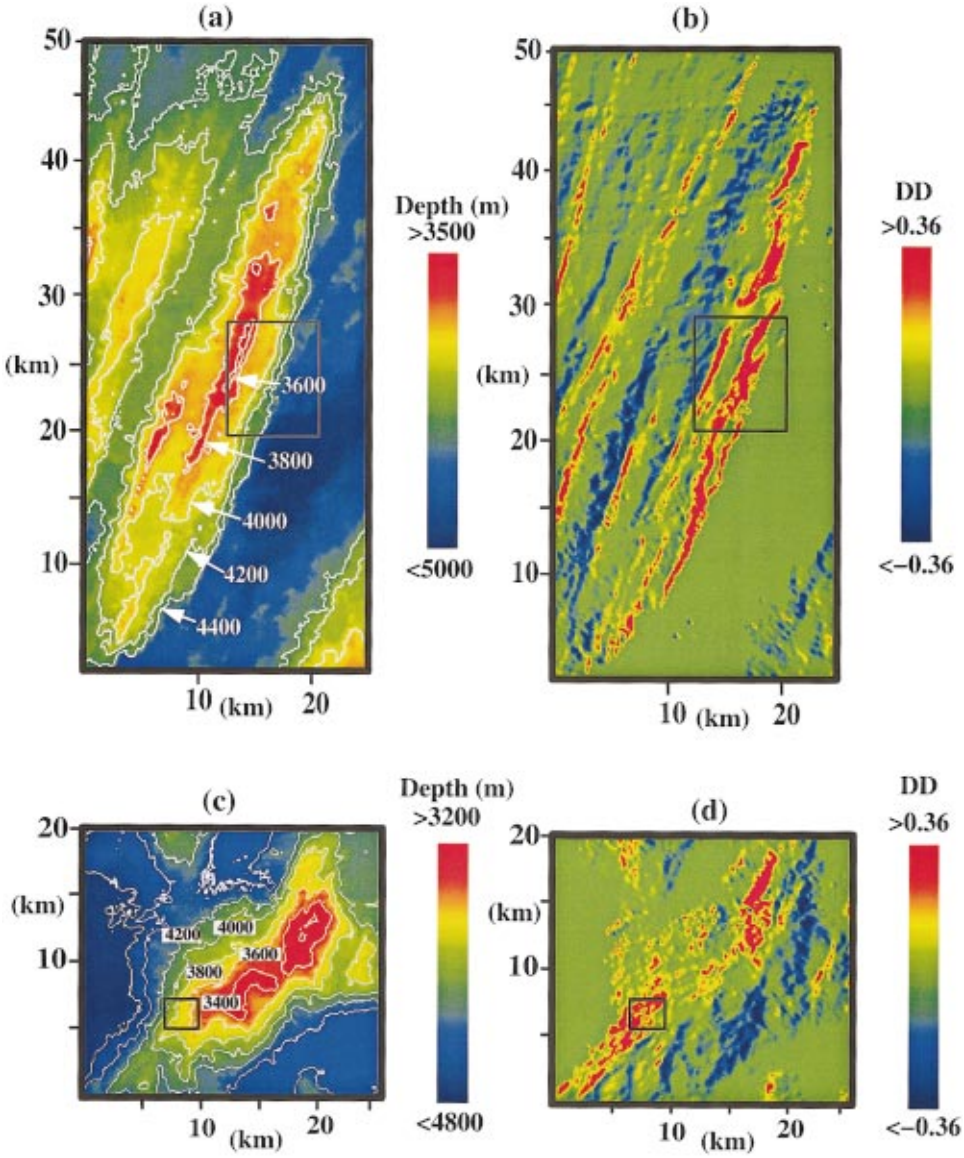


FIG. 2. Comparison between of the B′ and C′ bathymetric features and their directional derivatives (DD) charts. (a) The bathymetry of the B′ abyssal hill plotted at 200-m resolution. (b) The DD of B′ with respect to source at Easternstar center. (c) The bathymetry of the C′ abyssal hill plotted at 200-m resolution. (d) The DD of C′ with respect to source at the Easternstar center.

comparing measurements with different TL by providing a point of global convergence over all towed-array headings at the star centers. The CORY tracks for runs 3 and 8, at $\frac{1}{2}$ CZ from C′, and 5a and 5b, at $\frac{1}{2}$ CZ from B′, are therefore referred to as the *Easternstar* and *Westernstar*, respectively.[4]

The CORY transmitted from a ten-element vertical line array (VLA) with on-axis source level calibrated to roughly 229 dB *re* 1 $\mu$Pa@1 m. This source was deployed with center at 181 m. It transmitted a variety of waveforms, including the linear frequency modulation (LFM) waveform, which swept across the 200–255-Hz frequency band in 5 s, that is used exclusively in the present analysis. During each LFM transmission interval, acquired reverberation data were assigned a *data segment number* to identify the corresponding transmission cycle. Reverberation returned from each ocean ridge was received by the CORY's 128-element horizontal line array (HLA) at 170-m depth, in an effectively monostatic manner since the CORY source and receiver arrays were separated by roughly 1.12 km from array center to array center. The ALLIANCE HLA was towed at an average depth of 460 m for the bistatic receptions. Although the ALLIANCE source was also deployed in these experiments, we did not analyze data associated with it since its source strength and directivity was much lower than that of CORY. Specifically, only the CORY LFM transmissions, at the center frequency of 227.5 Hz, have been analyzed since they provide the best range resolution of ~14 m. The match-filtered data are averaged over 0.0625 s for CORY's receptions and 0.0533 s for ALLIANCE's receptions, and the effective range resolutions for the two towed-array systems are computed to be roughly 47 and 40 m, respectively.[4]

The geomorphology and gradient components of the B′ and C′ abyssal hills are shown in Fig. 2. While B′ has the classic elliptical shape, with high aspect ratio and long lineated scarps running parallel to its ridge axis, that typifies most abyssal hills of OC crust, C′ appears dome-like and dominated by normal faults with variable orientations, as is common among abyssal hills of IC crust. The structural difference between these two abyssal hills of distinct class can be better illustrated by bathymetric slope gradients components along the path sound travels or directional derivatives (DDs).[3,4,13] The DD is here defined as the inner product of

the bathymetric gradient with a local unit vector pointing in the horizontal direction of the source or receiver. In Fig. 2(b), where the DD is taken with respect to the Easternstar Center, the two major scarps on the eastern face of B′ appear prominently along the abyssal hill's major axis as lineations of high positive DD. By contrast, as shown in Fig. 2(d) where DD is again taken roughly with respect to the Easternstar Center, positive DD of C′ appears speckled and irregularly scattered over the entire ridge in accordance with its irregularly oriented faults. Besides the structural differences, the crustal composition of B′ and C′ is expected to be different since inside corners like C′ typically consist of plutonic rocks and mantle ultramafics such as peridotites and serpentinites,[5] while B′ is comprised of basalt thickly coated with iron–manganese.[7]

## III. THE EFFECT OF BATHYMETRIC UNDERSAMPLING ON SCATTERING DISTRIBUTION ESTIMATION AT B′

### A. Comparison of the 5-m resolution and 200-m resolution images

The effect of bathymetric undersampling on bistatic scattering analysis is evaluated using two different resolutions of bathymetry data for the B′ abyssal hill. Lower resolution (200-m sampled) hydrosweep data is taken from the precise $8\times9$ km region on the east-central face of B′ where the high-resolution (5-m sampled) bathymetry data are available. The exact 5-m resolution contours, for DD$>\frac{1}{2}$, used in Ref. 3 to designate the B′ scarps, were mapped point-to-point onto the 200-m grid chart. For comparison, the shaded relief plots at 5-m and 200-m resolutions for a section of the upper scarp are shown in Figs. 3(a) and (b), respectively. In the 5-m resolution plot, steep slopes and small 200-m scale anomalies, such as canyons and gullies, are clearly observed along the upper scarp. In the 200-m resolution plot, the upper scarp appears relatively flat over the sonar resolution footprint,[3] and small-scale anomalies are not properly resolved. Typical slopes on the B′ upper and lower scarps exceed 50° according to the 5-m sampled bathymetry, as shown in Fig. 2(b) of Ref. 3 and Fig. 22 of Ref. 4, but are significantly underestimated in the 200-m resolution bathymetric data set where the maximum slopes are found to be roughly 20°.

Two-way transmission loss (TL) and surface projection factors are computed over the resultant $8\times9$-km region using the same method as described in Ref. 3 but now with the lower resolution bathymetry sampled at 200 m. The parabolic equation is used to compute the two-way TL and a ray-trace method is used to model refraction due to depth-dependent sound-speed variations in the water column so that two-way travel time can be converted to range for reverberation charting. Rays are also traced to determine the incident angle $\theta_i$ from the source to the seafloor patch and the scattered angle $\theta_r$ from the seafloor to the receiver. These angles are measured relative to the seafloor normal. The seafloor's surface projection terms in the direction of incident and scattered rays are computed as in Ref. 3 via $C_i = 10\log(\cos\theta_i)$ and $C_r = 10\log(\cos\theta_r)$, respectively. To provide an illustrative example, surface projection and two-way TL charts obtained using bathymetry data sampled at 5-m and 200-m resolutions are shown in Fig. 4 for data segment S435.

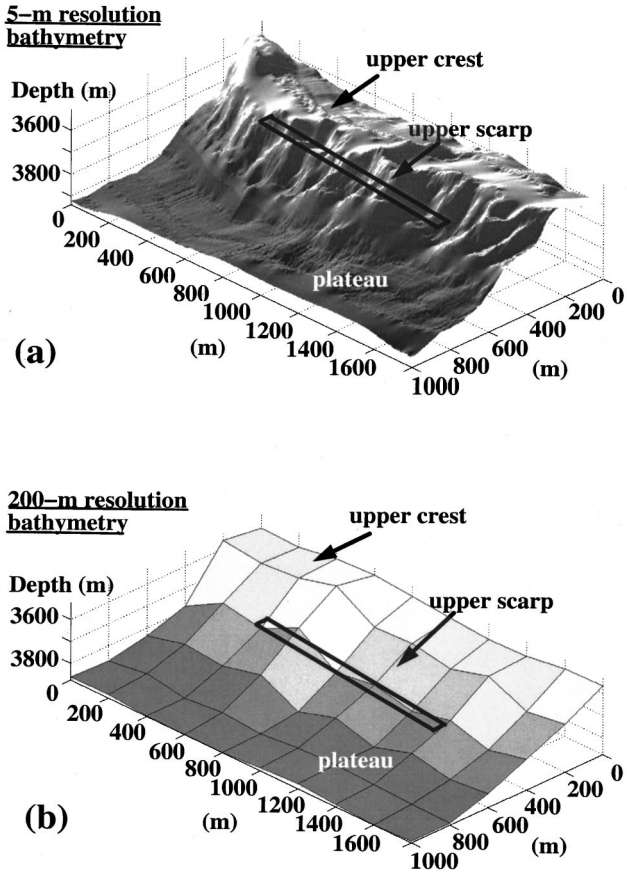


FIG. 3. Shaded relief plots for a section of the upper scarp at (a) 5-m resolution, and (b) 200-m resolution. Overlain is a typical sonar resolution footprint for monostatic reception at $\frac{1}{2}$ CZ with receiving array parallel to ridge axis. While the small-scale anomalies along the scarps such as canyons and gullies are clearly observed at 5-m resolution, these anomalies are not properly resolved at 200-m resolution. Slopes on such scarps are found to be severely underestimated in the 200-m resolution bathymetry.

Figures 4(a) and (b) illustrate the surface projection, $C_i = 10\log(\cos\theta_i)$, computed at two resolutions over the designated $8\times9$-km scarp area. Since the upper and lower scarps of B′ have slopes that typically exceed 50°, their surface projections in the 5-m resolution chart appear mostly in red, which correspond to values close to 0 dB. The surface projections of the two scarps in the 200-m resolution chart are well below 0 dB due to their underestimated slopes. The plateaus register with extremely low surface projections, as expected. Figures 4(c) and (d) compare two-way TL charted for S435 monostatic reception at 200-m and 5-m resolutions, respectively. While the details are lost when lower-resolution bathymetry is used, and these same details are averaged over in wide-area towed-array resolution footprints, the overall TL levels are similar for both high- and low-resolution bathymetry.

### B. Measured and modeled reverberation at B′

Modeled reverberation is computed by the same method and for the same regions and segments as in Ref. 3, again

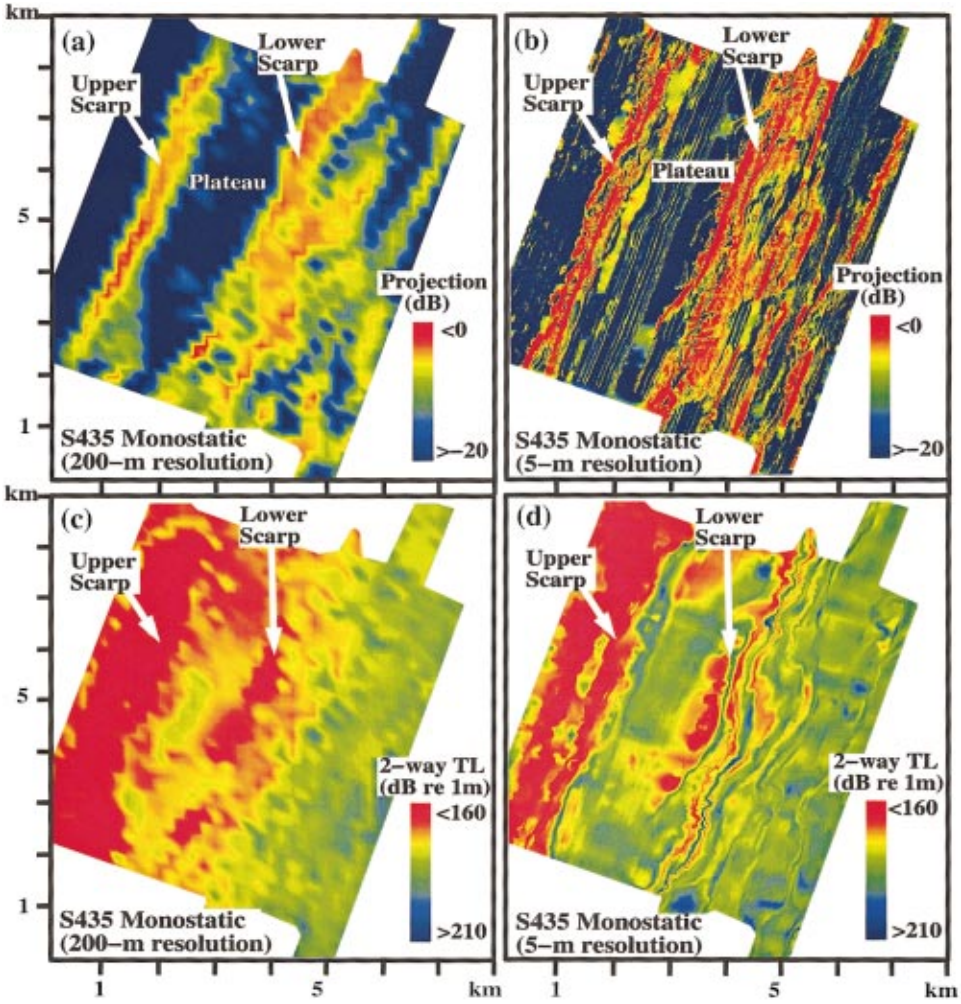


FIG. 4. Surface projection, $C_i = 10\log(\cos\theta_i)$, computed over the upper and lower scarps of B′ using (a) 200-m resolution, and (b) 5-m resolution bathymetry data for S435. The two steep scarps of B′ are undersampled at 200-m resolution and so, besides appearing blurry, yield significantly lower surface projections than at 5-m resolution. (c) and (d) show the two-way TL charts computed over the same site for 200-m and 5-m resolutions, respectively, for S435. Both the transmission losses computed over the scarp area are found to be similar in magnitudes, although detail is lost at 200-m resolution.

assuming a perfectly reflecting Lambertian surface, with unity albedo, except that 200-m sampled bathymetry is used instead of the 5-m sampled bathymetry. Since the 200-m grid size exceeds the towed-array range resolution of 40–47 m, there is no averaging of data over bathymetric range cells when performing the spatial convolution at 200-m resolution. Consequently, the modeled reverberation over the two scarps, shown for S435 in Fig. 5(b), has a more speckled appearance in the 200-m resolution charts than in the corresponding 5-m resolution charts, as shown for S435 in Fig. 12 of Ref. 3.

Prominent measured and modeled returns from the scarp areas show a good correlation at 200-m resolution, as shown for example in Fig. 5, just as they do for 5-m resolution, as shown for the same segment S435 in Fig. 12 of Ref. 3. While the model predicts strong lineated echoes to be returned along the scarp axes in the monostatic reception, Fig. 5(b), a speckle-like echo pattern across the two scarps is predicted in the corresponding bistatic reception, in Fig. 5(d), as described previously in Ref. 3. The general character of prominent returns measured over the two scarps, as illustrated in Figs. 5(a) and (c), agrees well with the predictions.

### C. Biazimuthal scattering distributions of the two B′ scarps

As demonstrated in Ref. 3, the scarp elevation within the sonar resolution footprint cannot be approximated as a planar surface since there is no unique surface normal to characterize the multiple bathymetric features within the resolution footprint. It is therefore meaningless to plot the estimates of scattering strength as a function of incident and scattered angles. Instead, the statistical approach adopted in Ref. 3 is used to describe the mean scattering distribution over the B′ scarps as a function of receiver azimuth $\Omega_r$, with respect to the normal horizontally bisecting the B′ scarp axis. The strength of the biazimuthal scattering distribution is averaged over the designated area according to Eq. (A5) of the Appendix. A full biazimuthal description of the scattering distribution over the B′ scarps, with respect to source and receiver azimuths, can be regained by referring to the distribution plot of source–receiver location pairs in Fig. 3 of Ref. 3. The biazimuthal scattering distribution strength is computed just as in Ref. 3 except that 200-m resolution bathymetry data is used instead of 5-m resolution data.

In Figs. 6(a) and (b), the curves of the mean measured reverberation level, at 200-m resolution, over the upper scarp $\langle R(x,y|\Omega_i,\Omega_r)\rangle_{A_{\rm up}}$ and the lower scarp $\langle R(x,y|\Omega_i,\Omega_r)\rangle_{A_{\rm low}}$ are plotted as a function of receiver azimuth $\Omega_r$ together with their standard deviations $\sigma_{A_{\rm up}}\{R(x,y)\}$ and $\sigma_{A_{\rm low}}\{R(x,y)\}$. The measured reverberation curve is computed via Eq. (A2) in the Appendix, and the subscripts $A_{\rm up}$ and $A_{\rm low}$ denote that the reverberation levels are averaged over the upper scarp and lower scarp areas, respectively. For

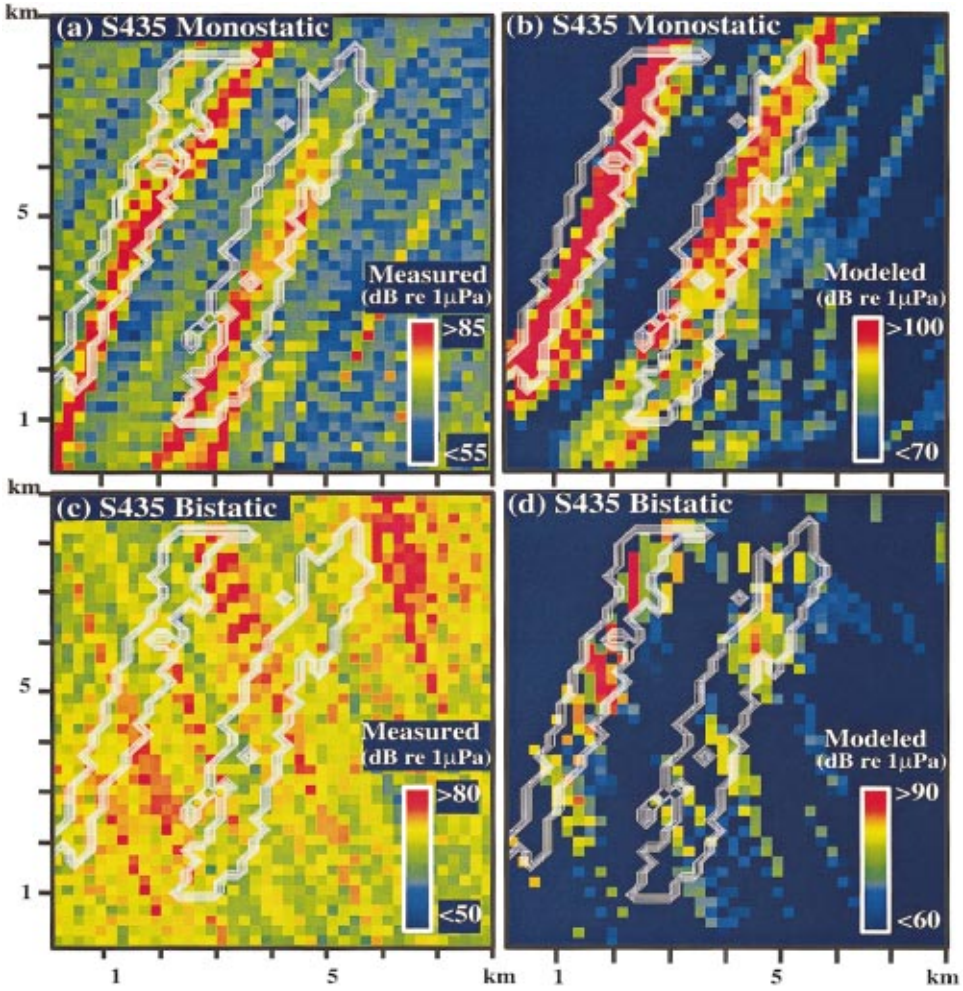


FIG. 5. Charts of monostatic and bistatic measured and modeled reverberation for S435 over the upper and lower scarp contours at 200-m resolution. (a) Measured monostatic reverberation. (b) Model monostatic reverberation. (c) Measured bistatic reverberation. (d) Modeled bistatic reverberation.

comparisons, the mean values of the 5-m resolution curves, previously obtained in Ref. 3, are plotted in dotted lines overlain in the same figure. Generally, these reverberation curves at 5-m and 200-m resolutions are found to be relatively constant across the $\pm 90°$ receiver azimuths, and their respective mean values closely match.

Curves of the mean reverberation level modeled over the two scarps, $\langle R_M(x,y|\Omega_i,\Omega_r)\rangle_{A_{\rm up}}$ and $\langle R_M(x,y|\Omega_i,\Omega_r)\rangle_{A_{\rm low}}$, are plotted as a function of receiver azimuth $\Omega_r$ in Figs. 7(a) and (b). The modeled reverberation curve is obtained using Eq. (A3) of the Appendix. Again, the modeled reverberation curves at 200-m resolution (in solid lines) exhibit the same trend as the 5-m resolution curves (in dotted lines) across receiver azimuth but are uniformly lower by several dB. While the mean values for the upper scarp at both resolutions fluctuate within $|\Omega_r|<30°$, the mean values for the lower scarp display a slight convex behavior with peak values within $|\Omega_r|<30°$ and roll off by $\sim$10 dB towards the extreme azimuths. It can also be easily seen that the 200-m resolution curves for the two scarps are distinctly lower than their corresponding 5-m resolution curves. The offset between the 200-m and 5-m resolution curves can be explained by examining the surface projection and two-way TL prior to the spatial convolution.

Figure 8 shows the mean surface projections $\langle C_i(x,y|\Omega_i,\Omega_r)+C_r(x,y|\Omega_i,\Omega_r)\rangle_{A_{\rm up}}$ and $\langle C_i(x,y|\Omega_i,\Omega_r)+C_r(x,y|\Omega_i,\Omega_r)\rangle_{A_{\rm low}}$ over the upper and lower scarps as a function of receiver azimuth $\Omega_r$. The surface projection curves, at 200-m resolution, exhibit the same convex behavior as the 5-m resolution curves, with their peak values near to the origin. However, the 200-m resolution curves are found to be roughly 6 to 8 dB lower than the mean surface projections at 5-m resolution. This offset is directly caused by the use of the undersampled 200-m resolution bathymetry data, where the projected area of the B′ scarps, with respect to the refracted ray paths, is highly underestimated.

The mean two-way TL, $\langle \mathrm{TL}_i(x,y|\Omega_i,\Omega_r)+\mathrm{TL}_r(x,y|\Omega_i,\Omega_r)\rangle_{A_{\rm up}}$ and $\langle \mathrm{TL}_i(x,y|\Omega_i,\Omega_r)+\mathrm{TL}_r(x,y|\Omega_i,\Omega_r)\rangle_{A_{\rm low}}$, are plotted as a function of receiver azimuth $\Omega_r$ in Fig. 9. The two-way TL curves, at 200-m resolution, match the 5-m resolution curves almost precisely, both in terms of their mean values and standard deviations at each receiver azimuth. The difference observed in the modeled reverberation curves at 5-m and 200-m sampling is then a direct consequence of the surface projection underestimate caused by the use of undersampled bathymetry.

The mean strengths of the biazimuthal scattering distributions estimated at 200-m resolution over the upper scarp $\langle \hat{\tilde{F}}(x,y|\Omega_i,\Omega_r)\rangle_{A_{\rm up}}$ and lower scarp $\langle \hat{\tilde{F}}(x,y|\Omega_i,\Omega_r)\rangle_{A_{\rm low}}$ are plotted as a function of receiver azimuth $\Omega_r$ in Fig. 10, along with their standard deviations $\sigma_{A_{\rm up}}\{\hat{\tilde{F}}(x,y)\}$ and

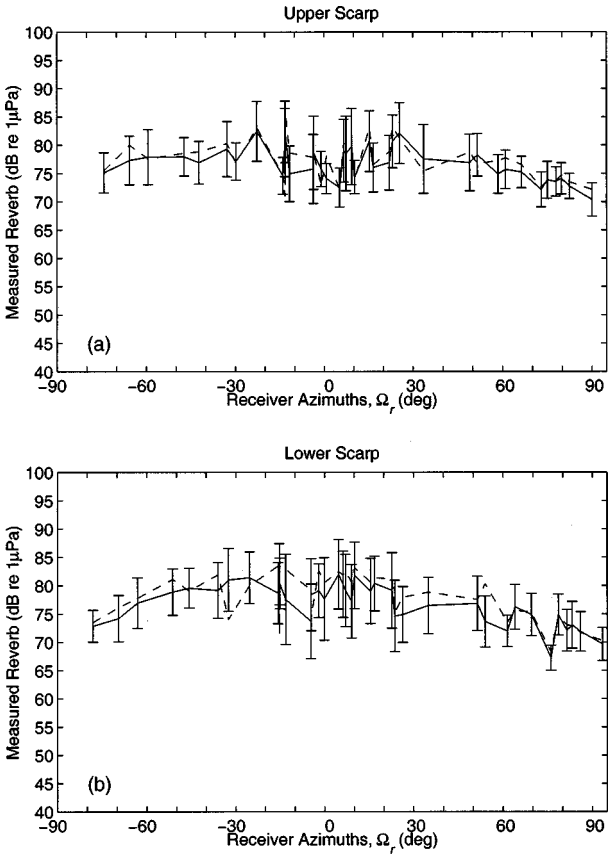


FIG. 6. Mean reverberation levels measured over (a) the upper scarp $\langle R(x,y|\Omega_i,\Omega_r)\rangle_{A_{\rm up}}$ and (b) the lower scarp $\langle R(x,y|\Omega_i,\Omega_r)\rangle_{A_{\rm low}}$ as a function of receiver azimuth $\Omega_r$ along with their respective standard deviations $\sigma_{A_{\rm up}}\{R(x,y)\}$ and $\sigma_{A_{\rm low}}\{R(x,y)\}$. Solid line denotes the 200-m resolution curve, and dotted line denotes the 5-m resolution curve.

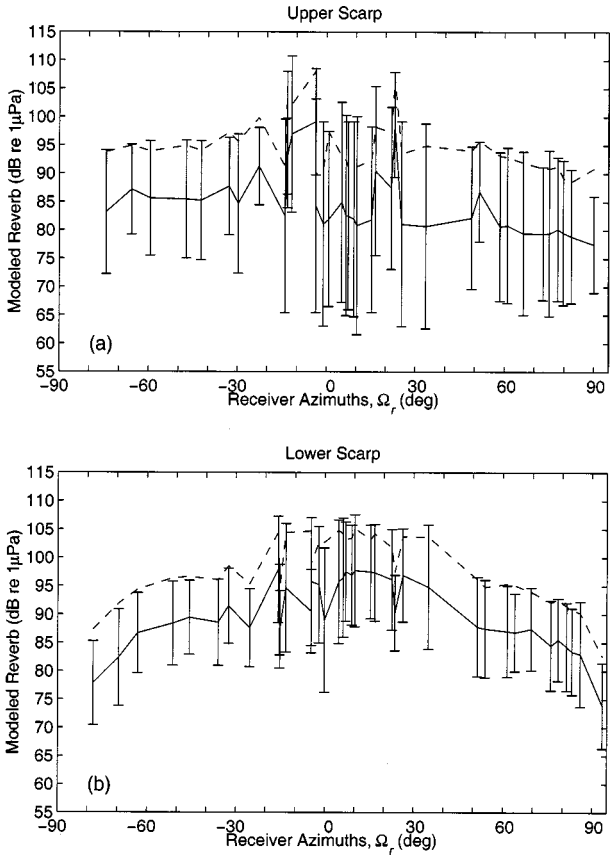


FIG. 7. Mean reverberation levels modeled over (a) the upper scarp $\langle R_M(x,y|\Omega_i,\Omega_r)\rangle_{A_{\rm up}}$, and (b) the lower scarp $\langle R_M(x,y|\Omega_i,\Omega_r)\rangle_{A_{\rm low}}$ as a function of receiver azimuth $\Omega_r$ along with their respective standard deviations $\sigma_{A_{\rm up}}\{R_M(x,y)\}$ and $\sigma_{A_{\rm low}}\{R_M(x,y)\}$. Solid line denotes the 200-m resolution curve, and dotted line denotes the 5-m resolution curve.

$\sigma_{A_{\rm low}}\{\hat{\tilde{F}}(x,y)\}$. The 200-m resolution curves again show the same constant trend as the 5-m resolution curves but are uniformly about 6 dB higher in level. Specifically, a constant line can be drawn within the error bars across receiver azimuth for curves of both upper and lower scarp scattering distribution strength for both 200-m resolution and 5-m resolution results, but the line is at roughly $-11$ dB in the former and $-17$ dB in the latter case. This overestimate in scattering distribution strength at 200-m resolution is a direct consequence of the underestimate in surface projected area caused by use of the undersampled 200-m resolution bathymetry. The use of bathymetry that undersamples the projected area of the seafloor within the resolution footprint of the towed-array system can lead to significant overestimates in the strength of seafloor scattering.

## IV. ANALYSIS OF BISTATIC SCATTERING FROM C′ WITH 200-m RESOLUTION BATHYMETRY

### A. Experiment geometry

The $3\times2$-km region designated for this study of bistatic scattering from the C′ abyssal hill is overlain on 200-m sampled bathymetry in Fig. 11(a). This site at the southwest corner of the roughly $10\times20$-km C′ is selected because it is consistently insonified by the main beam of the CORY source array throughout the experiments. As shown in the magnified plots of Fig. 11(a), the selected $3\times2$-km C′ region is part of a steep scarp that faces northwest with depths ranging from 4000 to 3500 m that include the source's conjugate depth of 3800 m[3,4,13] and so intersects the refractive path of sound from sources and to receivers at $\frac{1}{2}$ CZ stand-off range. The directional derivative of C′, shown in Fig. 11(b), is computed with the source located to the west of C′ within 1 km of the Eastern Star center at the CORY's position during S229 transmissions. The DD exhibits a speckled pattern consistent with the irregularly oriented faults known to characterize the geomorphology of C′.

The locations of the two research vessels for data segments analyzed in the C′ study are plotted in Fig. 12. The central black box in this figure indicates the $3\times2$-km area at the southwest (SW) corner of C′ designated for this study, to be referred to as the SW box. A total of 10 monostatic and 22 bistatic segments has been analyzed to cover a full suite of 180° bistatic angles distributed in a semicircle at roughly $\frac{1}{2}$ CZ radius from the center of SW box. The boxed alphabets indicate the RV CORY's locations, while the corresponding unboxed alphabets denote the RV ALLIANCE's locations for the same transmission.

The biazimuthal distribution of the source–receiver lo-

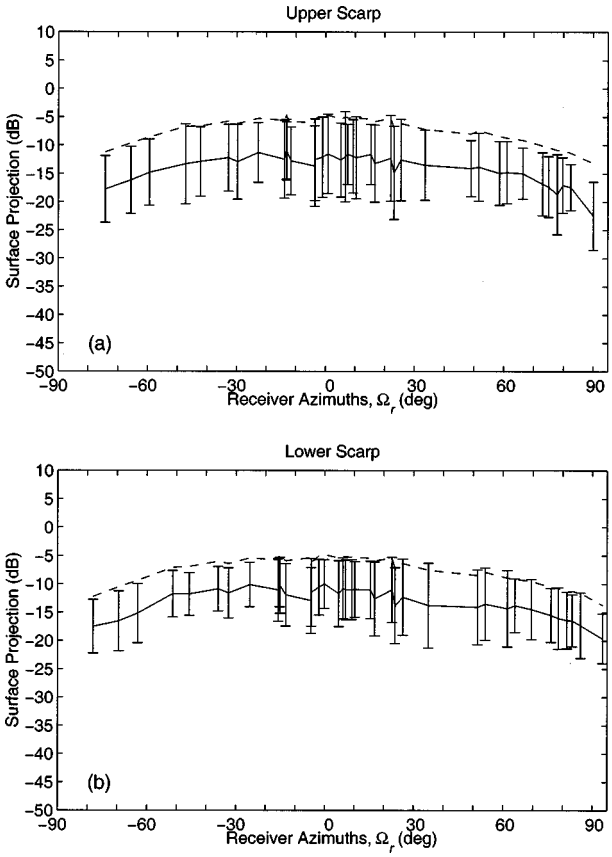


FIG. 8. The mean surface projection over (a) the upper scarp $\langle C_i(x,y|\Omega_i,\Omega_r)+C_r(x,y|\Omega_i,\Omega_r)\rangle_{A_{\rm up}}$, and (b) the lower scarp $\langle C_i(x,y|\Omega_i,\Omega_r)+C_r(x,y|\Omega_i,\Omega_r)\rangle_{A_{\rm low}}$ as a function of receiver azimuth $\Omega_r$ along with their standard deviations. Solid line denotes the 200-m resolution curve, and dotted line denotes the 5-m resolution curve.

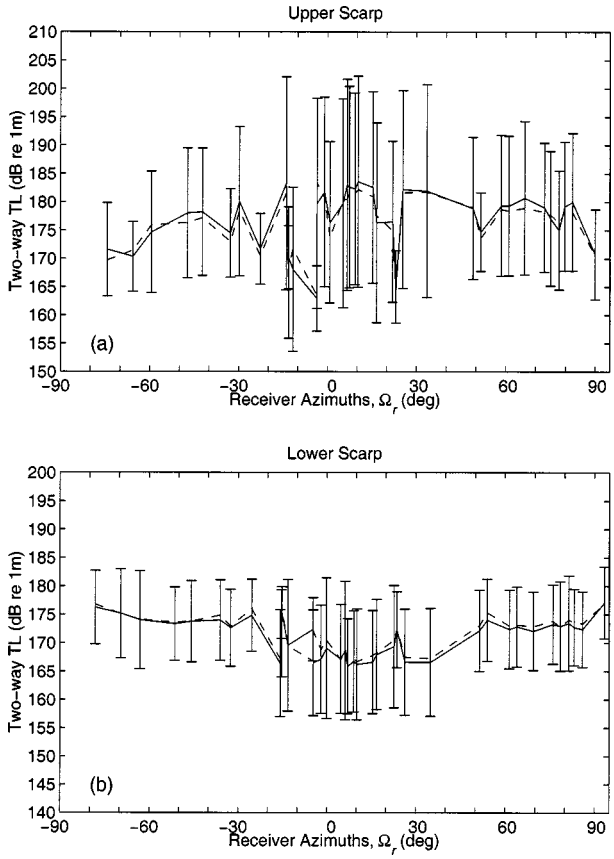


FIG. 9. The mean two-way transmission loss over (a) the upper scarp $\langle \mathrm{TL}_i(x,y|\Omega_i,\Omega_r)+\mathrm{TL}_r(x,y|\Omega_i,\Omega_r)\rangle_{A_{\rm up}}$, and (b) the lower scarp $\langle \mathrm{TL}_i(x,y|\Omega_i,\Omega_r)+\mathrm{TL}_r(x,y|\Omega_i,\Omega_r)\rangle_{A_{\rm low}}$ as a function of receiver azimuth $\Omega_r$ along with their standard deviations. Solid line denotes the 200-m resolution curve, and dotted line denotes the 5-m resolution curve.

cation pairs is plotted in Fig. 13. Azimuth is measured counterclockwise from a northwest line that originates at the center of the SW box and is normal to the scarp axis. Specifically, the source azimuth $\Omega_i=0°$ falls on this line which connects the RV CORY's location for segment S229 to the center of the SW box, as indicated by the dotted line between F and C′ in Fig. 12 which bisects the *Easternstar* ship tracks. While the source azimuths $\Omega_i$ fall within $|\Omega_i|<30°$, the receiver azimuths $\Omega_r$ span over a $\pm 90°$ sector for a complete study of biazimuthal scattering at C′.

### B. Wide-area bistatic images

Monostatic and bistatic reverberation charts for S229, S874, and S883 are shown in Figs. 14, 15, and 16, respectively. ALLIANCE was located west of C′ in S874, midway to the northern extreme of its course in S229, and near the southern extreme in S883, with source–receiver pairs distributed according to $\Omega_i\sim 0°$, $\Omega_r\sim -57°$ for S229, $\Omega_i\sim 25°$, $\Omega_r\sim 37°$ for S874, and $\Omega_i\sim 7°$, $\Omega_r\sim 69°$ for S883. These distinct bistatic locations along with their distinct towed-array headings lead to reverberation charts that are highly representative of the various geometrical issues at play in the present experiment.

In Figs. 14(a) to 16(a), prominent echoes are primarily charted over the western scarps of C′ in the vicinity of the conjugate depth contour. Since the CORY's source and its towed-array receiver are close to each other, ~1.2 km, with respect to their respective $\frac{1}{2}$ CZ ranges to C′, reception by CORY is effectively monostatic and so reverberation charts exhibit circular symmetry about the source/receiver location. Echo returns are ambiguously mirrored across the CORY receiver's axis due to the inherent left–right ambiguity of the linear towed array.[3,4,13,14] Differences in charted reverberation across the segments arise primarily from changes in TL and projected area associated with changes in CORY position.

The bistatic reverberation charts, in Figs. 14(c), 15(c), and 16(c), illustrate three typical scenarios in bistatic sonar reception. In S874, a circularly symmetric pattern arises as in monostatic reception since the separation between the RV CORY and ALLIANCE is relatively short (~6 km) compared to the range to C′. Moreover, the ambiguous returns are reflected across the ALLIANCE receiving array axis with near-perfect symmetry. In S883, reverberation arriving at the same travel time follows elliptical arcs about foci located at the well-separated source and receiver locations. Left–right ambiguity is relatively symmetric for S883 because the ALLIANCE receiver's heading coincides with the source–receiver axis. The ambiguous image of C′ then occupies a similar spatial area as the true one. In S229, the separation

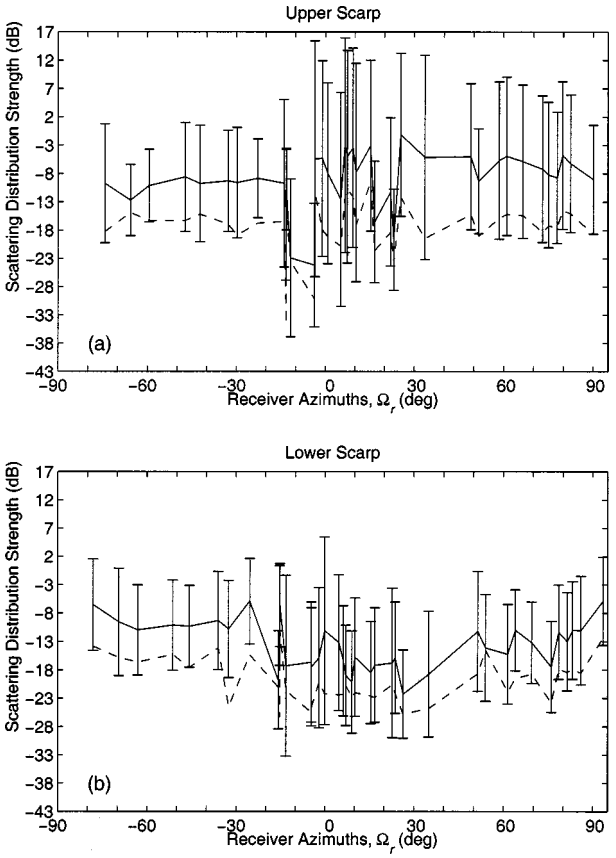


FIG. 10. The mean strength of the biazimuthal scattering distribution estimated over (a) the upper scarp $\langle \hat{\hat{F}}(x,y|\Omega_i,\Omega_r)\rangle_{A_{\rm up}}$, and (b) the lower scarp $\langle \hat{\hat{F}}(x,y|\Omega_i,\Omega_r)\rangle_{A_{\rm low}}$ as a function of receiver azimuth $\Omega_r$ along with their standard deviations $\sigma_{A_{\rm up}}\{\hat{\hat{F}}(x,y)\}$ and $\sigma_{A_{\rm low}}\{\hat{\hat{F}}(x,y)\}$. Solid line denotes the 200-m resolution curve, and dotted line denotes the 5-m resolution curve.

between CORY and ALLIANCE is again significant, but the ALLIANCE heading departs considerably from the source–receiver axis. This leads to an absence of symmetry about the receiver axis. The distortion compresses the C′ ambiguity to a much smaller spatial region than the true return. The C′ ambiguity also falls at a shorter range than the true return to preserve the two-way travel time. Similar behavior in wide-area bistatic reverberation charts has been documented previously at the B′ abyssal hill.[3]

Figures 14 to 16(b) and (d) illustrate the bistatic horizontal projection of bathymetry (BHBP), as defined in Ref. 3, computed over C′. Overlying the BHBP images are high-amplitude reverberation contours for the specified segment. Most of the western scarps of C′ register positive BHBP in the monostatic charts due to the CORY's predominantly western location. Prominent echoes register well with regions of positive BHBP. The BHBP for the bistatic charts varies significantly over the chosen three segments because of their differing source–receiver orientations. In the extreme case of S883, Fig. 16(d), only the SW corner of C′ yields positive BHBP, and consequently prominent returns, because the ALLIANCE has moved to the southwest of C′ and other portions of the abyssal hill are shadowed. The SW box is in this region and is almost always well insonified by the CORY's source and at the same time is acoustically visible to the ALLIANCE receiving array throughout the bistatic experiment at C′.

Wide-area images for all the data segments analyzed in this study have been examined to ensure that the inherent left–right ambiguity of the linear towed array did not corrupt the measured results over the designated SW box of C′. Although a few data segments, such as S220, S919, and

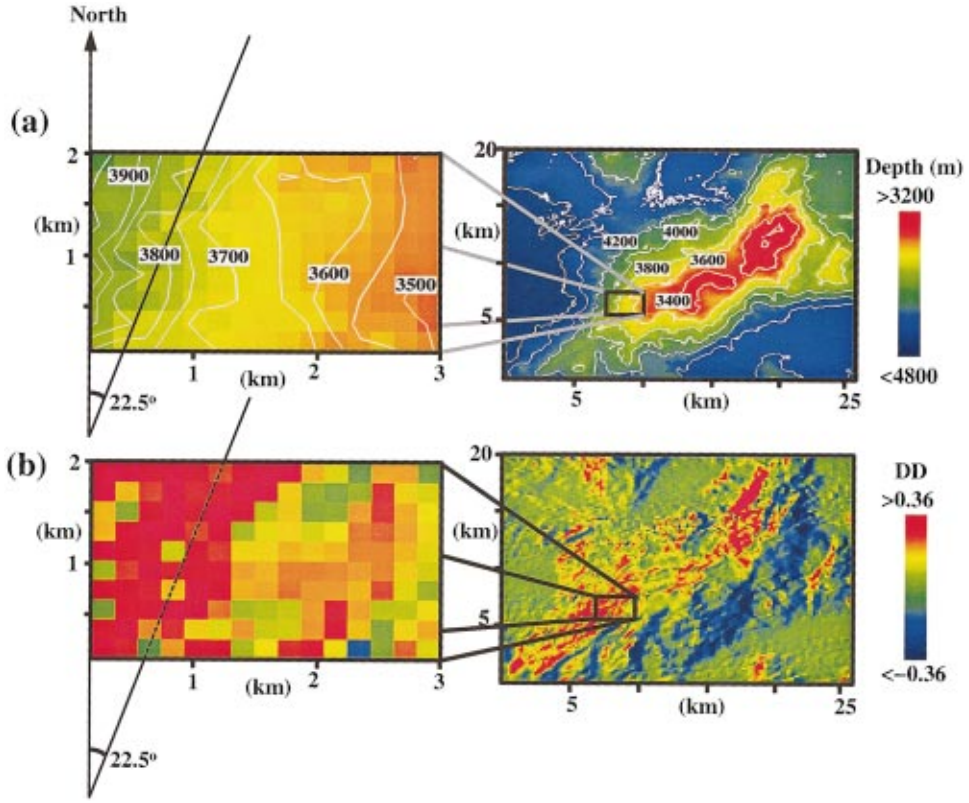


FIG. 11. (a) Bathymetry of the C′ inside corner abyssal hill sampled at 200-m intervals. The black box at the SW corner of C′ indicates the 3 ×2-km region designated for this study and subsequently referred to as the SW box. (b) The DD for C′ with respect to a source at the Easternstar center. Steep scarps facing the source are charted in red with DD>0.36, equivalent to slope gradients >20°; steep slopes facing away from the source are in blue. The axis of the scarps is at roughly 22.5° as shown.

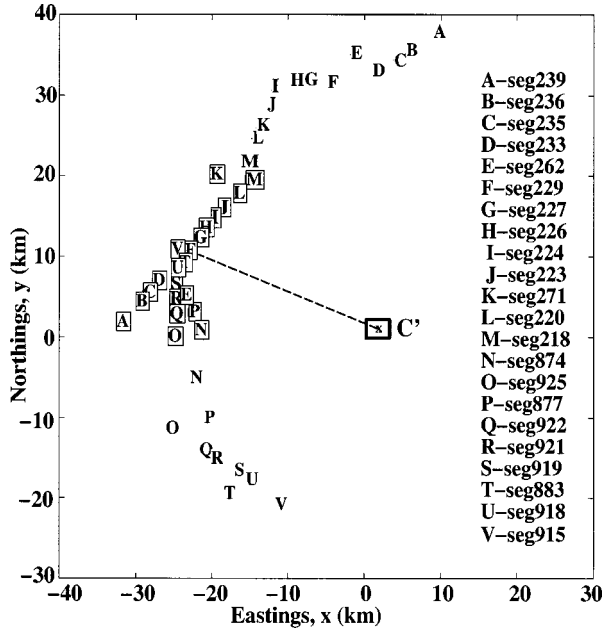


FIG. 12. Bistatic locations of the two research vessels during the LFM transmissions analyzed in the C′ study, given in Eastings and Northings. These locations are distributed in a semicircle about the center of SW box, which is the scarp area designated for the present study. The boxed alphabets denote the CORY's locations, i.e., the source locations, while the corresponding unboxed alphabets along the circular arc denote the ALLIANCE's locations, i.e., bistatic receiver locations, for the given transmission cycle.

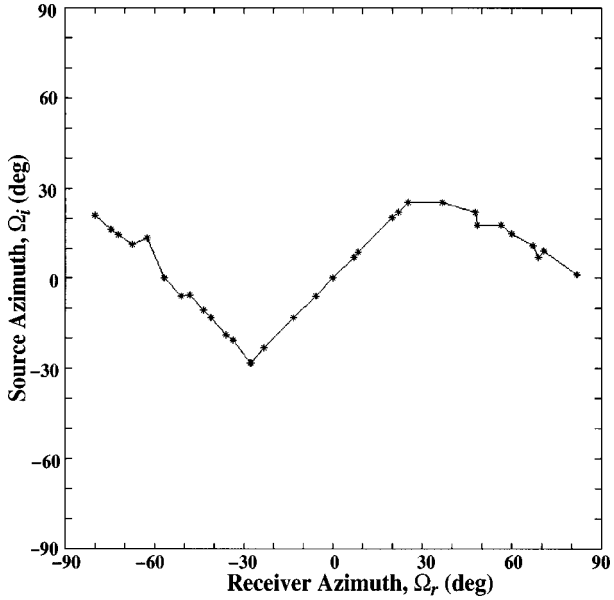


FIG. 13. Azimuthal distribution of the source and receiver pairs for the C′ study. While the source azimuths $\Omega_i$ fall within $|\Omega_i|<30°$, the receiver azimuths $\Omega_r$ span a full 180° range of nonforward azimuths about C′.

S925 monostatic segments, were found to have some ambiguities charted to the C′ ridge, these did not fall within the SW box.

### C. Measured and modeled reverberation at C′

Figure 17 shows the surface projection and TL at the SW corner of C′ for segment S229. Since the designated 3 $\times$2-km SW box cannot adequately display broad spatial variations of TL due to bathymetry, a 9$\times$6-km area is illustrated here to provide more perspective. Specifically, the SW box shown as the central white box in all the figures indicates the scarp area at C′ designated for the present analysis. Transmission loss from source to scattering patch, $TL_i$, and scattering patch to receiver, $TL_r$, is produced by sweeping the broadband TL maps, which are incoherently averaged over 200–255-Hz band as in Ref. 3, across the bathymetry of C′ at 200-m resolution. The surface projection terms from source to seafloor, $C_i$, and seafloor to receiver, $C_r$, are obtained by sweeping across the scarp area with grazing angle maps produced by ray trace, as in Ref. 3.

Figures 17(a) and (b) illustrate the surface projections within the SW box along ray paths directed towards the source and receiver's locations. In segment S229, the RV CORY is located at the SW corner's broadside, while the RV ALLIANCE is midway to the northern extreme of its path. As a result, the SW corner scarp of C′ projects larger surface area towards the CORY than towards the ALLIANCE. The areas of extremely low surface projection, in dark blue in the lower right corners of Figs. 17(a) and (b), are in the shadow zone of the refracted sound paths.

The transmission loss charts $TL_i$ and $TL_r$ in Figs. 17(c) and (d) illustrate the distinct natures of broadband TL maps for source versus receiver. Figure 17(c) illustrates well-structured main beam behavior. The SW box has a low $TL_i$ since it falls within the source's main beam, while the higher elevation above it suffers a high TL due to the shadow zone of the source main beam's refractive path. Figure 17(d) shows $TL_r$, from seafloor to the receiver, to be relatively constant across the site. Spatial variations in $TL_i$ are found to be more dominant than $TL_r$ in dictating the characteristics of the two-way TL across the SW corner of C′.

The measured and modeled reverberation charts for segments S229, S874, and S883 are presented in Figs. 18–20, respectively. Generally, prominent measured returns from the SW corner scarp of C′ show reasonably good agreement with corresponding modeled returns in the monostatic reverberation charts. Across these three segments, the character of reverberation changes predictably as a function of spatial variations of the TL and surface projection. For example, the model predicts correctly that the lower elevation of the SW corner scarp at C′ will return prominent echoes in S229 and S883 monostatic receptions, while it predicts higher elevations to return prominent echoes in S874 monostatic reception.

However, such a good visual correlation is sometimes not found in the bistatic reverberation charts over the SW corner box. Frequently, the modeled reverberation predicts strong echo returns from a specific area of the scarp, while the measured reverberation appears more diffusely scattered over the entire scarp area. This inconsistency has been explained in our B′ high-resolution study.[3] Specifically, the signal-dependent speckle noise arising from statistical fluctuations of the scattered field is sufficient to obscure the expected echo patterns. That is, within the insonified scarp, the detailed structure of bistatic returns has variations on the

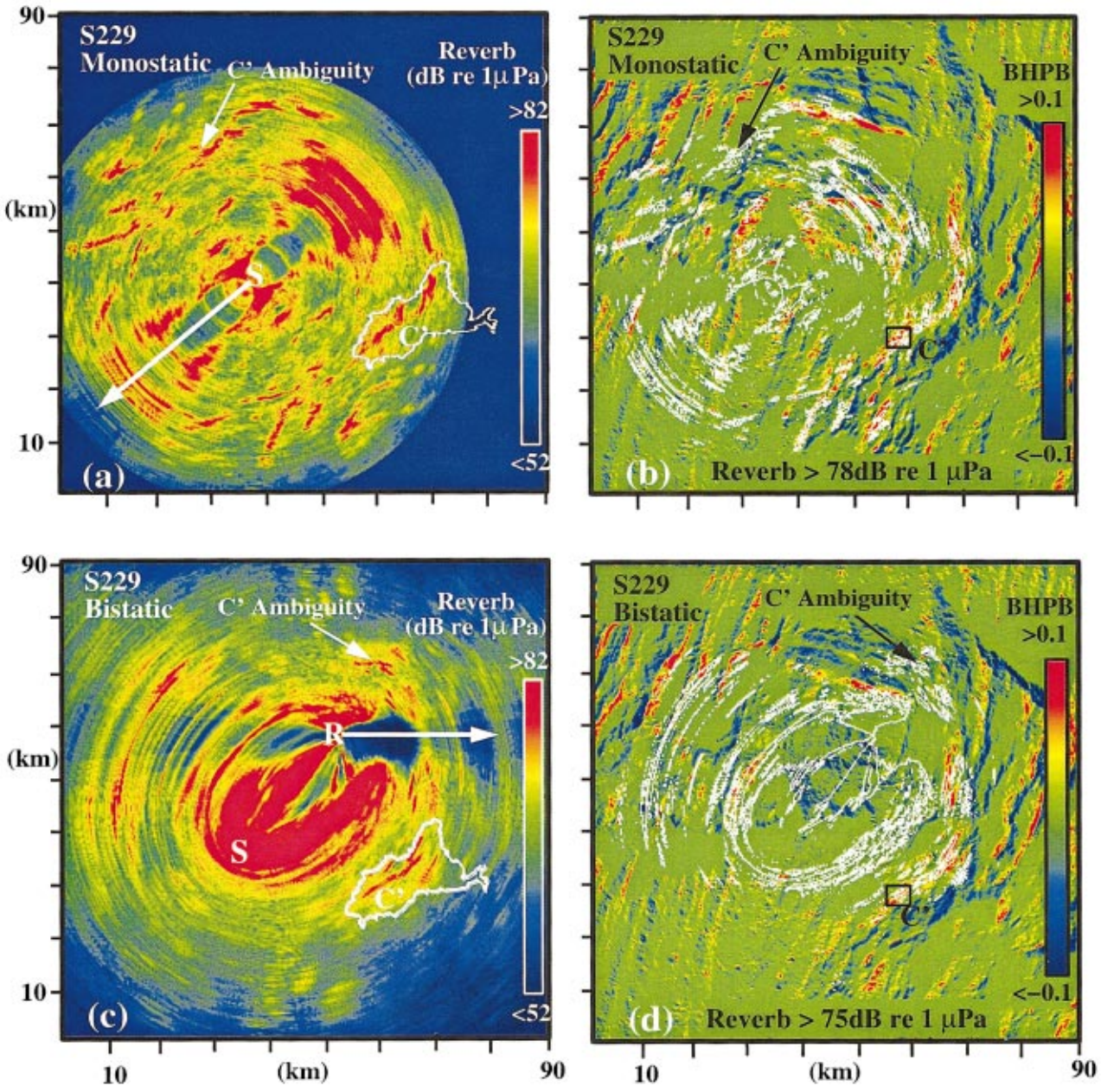


FIG. 14. Wide-area images of monostatic and bistatic reverberation measured for 200–255-Hz LFM S229. (a) Monostatic reverberation chart showing symmetry about the array axis for CORY heading at 228°. (b) Contours of high-level backscatter, overlain on the BHBP, coregister with major scarps on C′ facing the source–receiver. (c) Bistatic reverberation chart showing asymmetry about the ALLIANCE's array heading at 91°. (d) Contours of high-level backscatter overlain on the BHPB. The SW box is shown in black in (b) and (d).

order of the 5.6-dB standard deviation of speckle noise.[6] Since prominent echoes returned from the SW corner scarp are tens of dB higher than returns from neighboring scarps, the large-scale structure of the scarp can be imaged deterministically in both monostatic and bistatic receptions. There is also a possibility that the scarp area at C′ might contain some small-scale features, which are under-resolved at 200-m resolution, responsible for the scattered echo patterns observed in the bistatic charts. We have found no distinct correlation, however, between fine-scale scarp structure (<200-m scale) and fine-scale structure in prominent returns from the scarps in the B′ high-resolution study.[3] Nor should one be expected, since the expected variations of modeled reverberation along the B′ scarps are on the order of the 5.6-dB speckle noise standard deviation. Signal-dependent noise is therefore believed to be the most probable cause for the lack of fine-scale correlation between measured and modeled reverberation.

### D. Biazimuthal scattering distribution of the C′ scarp

Curves of the mean measured and modeled reverberation levels, computed at 200-m resolution over the SW box of C′, $\langle R(x,y|\Omega_i,\Omega_r)\rangle_{A_{C'}}$ and $\langle R_M(x,y|\Omega_i,\Omega_r)\rangle_{A_{C'}}$, are plotted as a function of receiver azimuth $\Omega_r$ in Figs. 21(a)

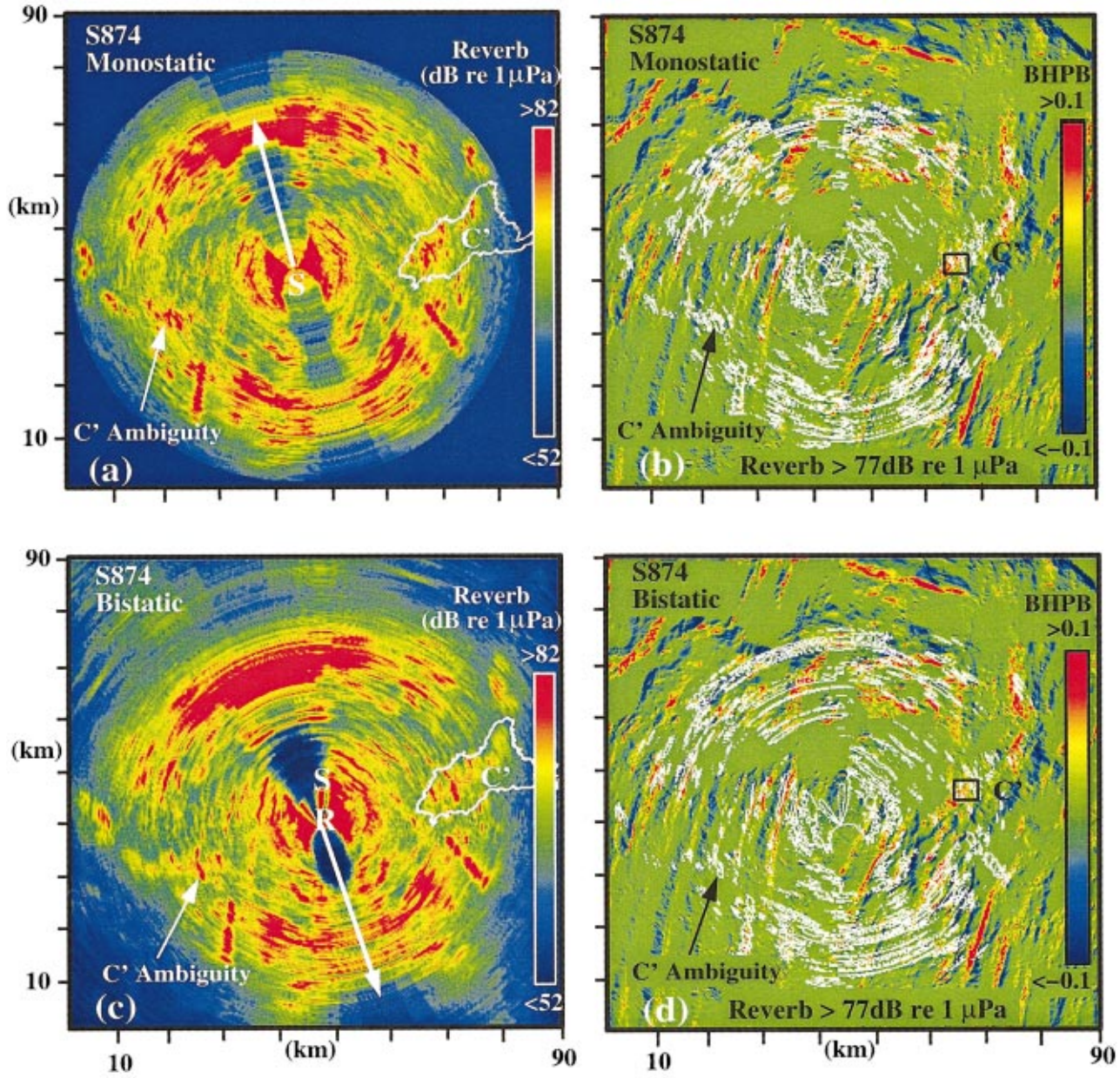


FIG. 15. Wide-area images of monostatic and bistatic reverberation measured for 200–255-Hz LFM S874. (a) Monostatic reverberation chart showing symmetry about the array axis for CORY heading at 345°. (b) Contours of high-level backscatter, overlain on the BHBP, coregister with major scarps on C′ facing the source–receiver. (c) Bistatic reverberation chart showing circular symmetry about the ALLIANCE's array heading at 162°. (d) Contours of high-level backscatter overlain on the BHPB.

and (b), along with their standard deviations $\sigma_{A_{C'}}\{R(x,y)\}$ and $\sigma_{A_{C'}}\{R_M(x,y)\}$. The subscript $A_{C'}$, which follows the same notation used in the B′ study, indicates that the measured and modeled reverberation are averaged over an area $A$, namely the SW corner scarp of C′. A full biazimuthal description of these parameters, with respect to source and receiver azimuths, can be regained by referring to the source–receiver location pairs as shown in Fig. 12.

The mean measured reverberation curve, in Fig. 21(a), shows a remarkably constant behavior across the receiver azimuths with standard deviation of roughly 5 dB. Compared to the B′ reverberation curves, the average level of the C′ curve is found to be lower by roughly 2 dB. In Fig. 21(b), the mean modeled reverberation curve displays relatively constant behavior, except at the extreme receiver azimuths, $\Omega_r < -60°$, where a roll-off of more than 10 dB is observed. This behavior can be explained by examining the surface projection and two-way TL terms.

Figure 22(a) illustrates the mean surface projection $\langle C_i(x,y|\Omega_i,\Omega_r)+C_r(x,y|\Omega_i,\Omega_r)\rangle_{A_{C'}}$ plotted as a function of receiver azimuth $\Omega_r$. A convex dependence is observed with standard deviations of roughly 6 dB across the receiver azimuths. The mean value peaks at −15 dB near the origin, and gradually rolls off to roughly −20 dB towards the two extremes. This convex behavior is expected since the SW box is comprised of a scarp that faces the center of Easternstar. Thus, the receiver azimuth at 0°, which corresponds to the RV CORY's location at the center of Easternstar, yields a

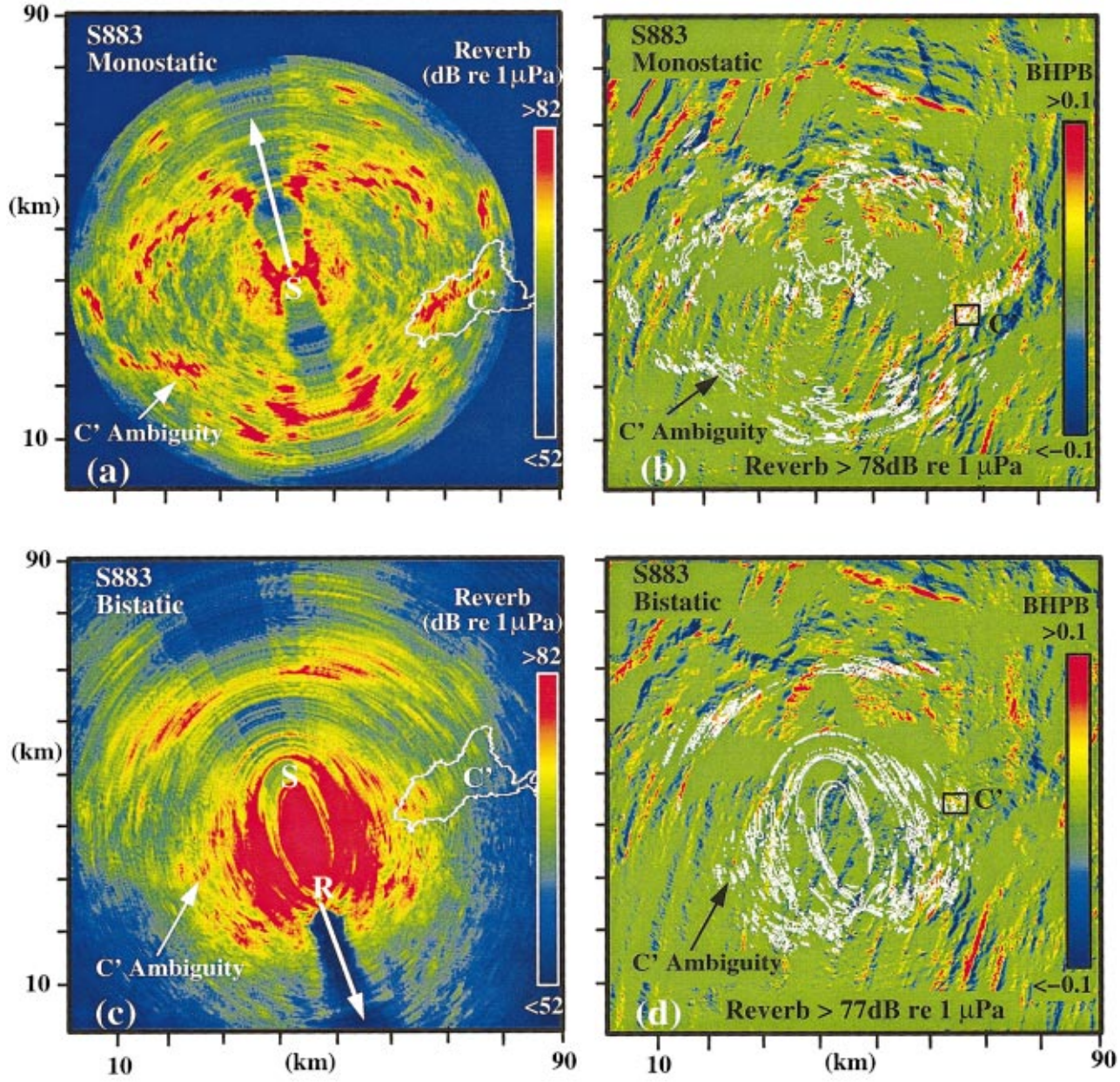


FIG. 16. Wide-area images of monostatic and bistatic reverberation measured for 200–255-Hz LFM S883. (a) Monostatic reverberation chart showing symmetry about the array axis for CORY heading at 346°. (b) Contours of high-level backscatter, overlain on the BHBP, coregister with major scarps on C′ facing the source–receiver. (c) Bistatic reverberation chart showing elliptical symmetry about the ALLIANCE's array heading at 163°. (d) Contours of high-level backscatter overlaid on the BHPB.

higher surface projection than the extreme receiver azimuths.

Figure 22(b) shows the two-way transmission loss $\langle \mathrm{TL}_i(x,y|\Omega_i,\Omega_r)+\mathrm{TL}_r(x,y|\Omega_i,\Omega_r)\rangle_{A_{C'}}$ plotted as a function of receiver azimuth $\Omega_r$. The mean two-way TL curve is relatively flat across the receiver azimuths, except for $\Omega_r < -60°$ where the curve rises up by more than 10 dB. Large two-way TL occurs at this azimuthal extreme because the upper elevation of the SW box apparently lies in the shadow zone of the source's main beam according to the 200-m sampled bathymetry. Lower elevations of the SW box, however, are well insonified by the source's main beam and have low TL. Consequently, a wide spread of TL occurs across these extreme azimuths which leads to large standard deviations in the two-way TL curve for $\Omega_r < -60°$. For $\Omega_r > -60°$, the entire SW box enjoys main-beam insonification and low TL. The modeled reverberation over the C′ scarp has also displayed similar characteristics as the measured reverberation, except for $\Omega_r < -60°$ where our model predicts a stronger shadowing effect than found in the data. This effect is likely due to the use of what is probably highly undersampled bathymetry in our modeling at C′.

The mean strength of the biazimuthal scattering distribution estimated over the C′ scarp, $\langle \hat{\tilde{F}}(x,y|\Omega_i,\Omega_r)\rangle_{A_{C'}}$, is plotted as a function of receiver azimuth $\Omega_r$ along with its standard deviation $\sigma_{A_{C'}}\{\hat{\tilde{F}}(x,y)\}$ in Fig. 23. The curve dis-

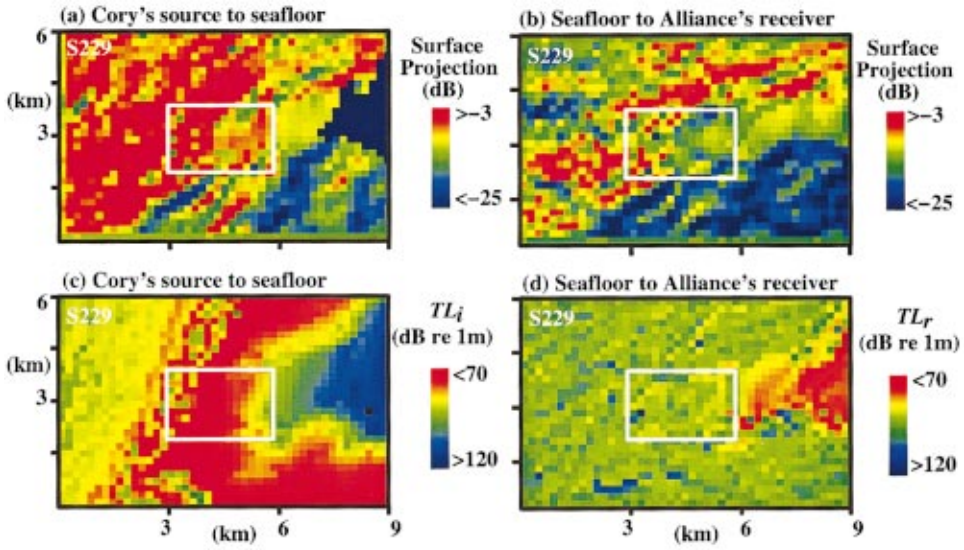


FIG. 17. Surface projection and one-way transmission loss charts computed over the SW corner of C′ for S229 transmission, including the SW box. (a) Surface projection $C_i = 10\log(\cos\theta_i)$ of bathymetry from source to seafloor using ray trace. (b) Surface projection $C_r = 10\log(\cos\theta_r)$ of bathymetry from seafloor to receiver using ray trace. (c) Transmission loss $TL_i$ from CORY source array to seafloor scattering patch. (d) Transmission loss $TL_r$ from seafloor to ALLIANCE receiver.

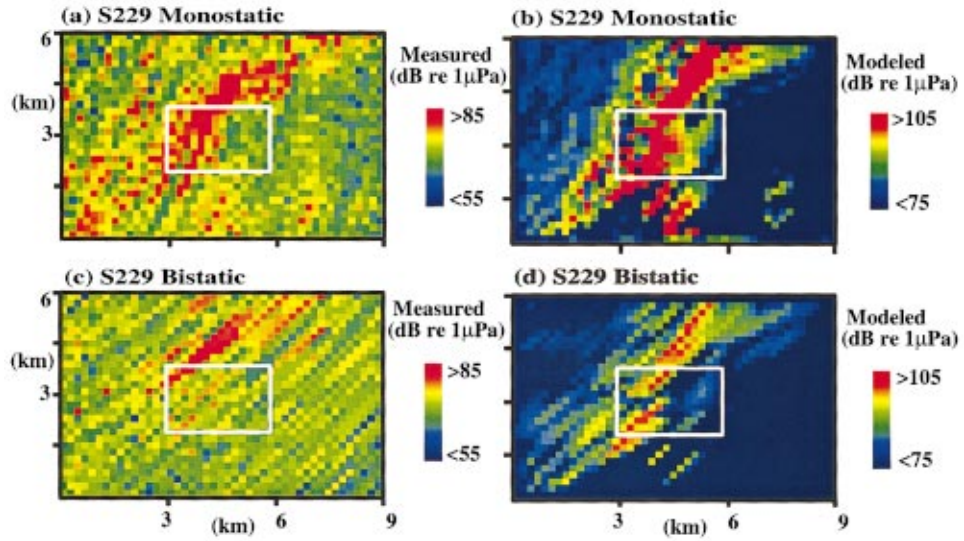


FIG. 18. Charts of the measured and modeled reverberation for S229 over the SW corner of C′ at 200-m resolution including the SW box. (a) Measured monostatic reverberation. (b) Modeled monostatic reverberation. (c) Measured bistatic reverberation. (d) Modeled bistatic reverberation.

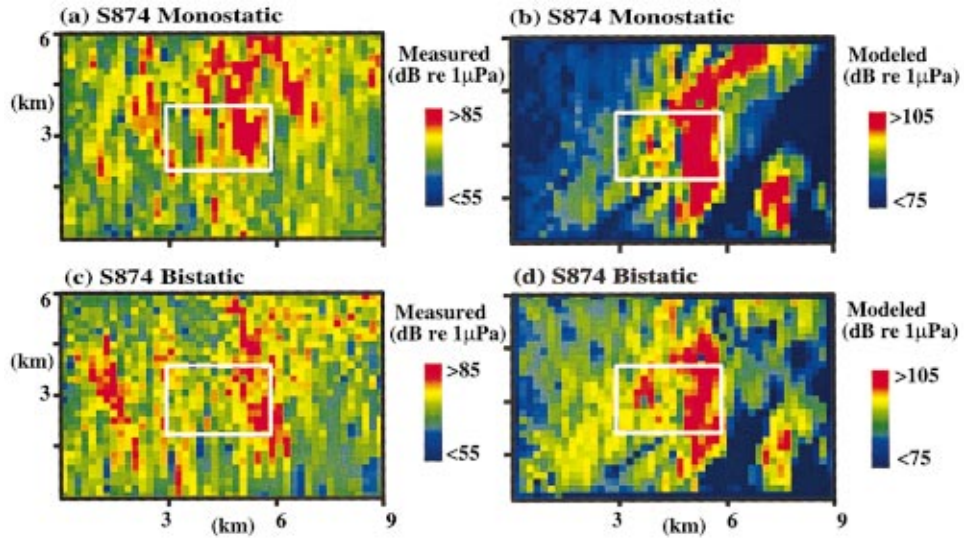


FIG. 19. Charts of the measured and modeled reverberation for S874 over the SW corner of C′ at 200-m resolution including the SW box. (a) Measured monostatic reverberation. (b) Model monostatic reverberation. (c) Measured bistatic reverberation. (d) Modeled bistatic reverberation.

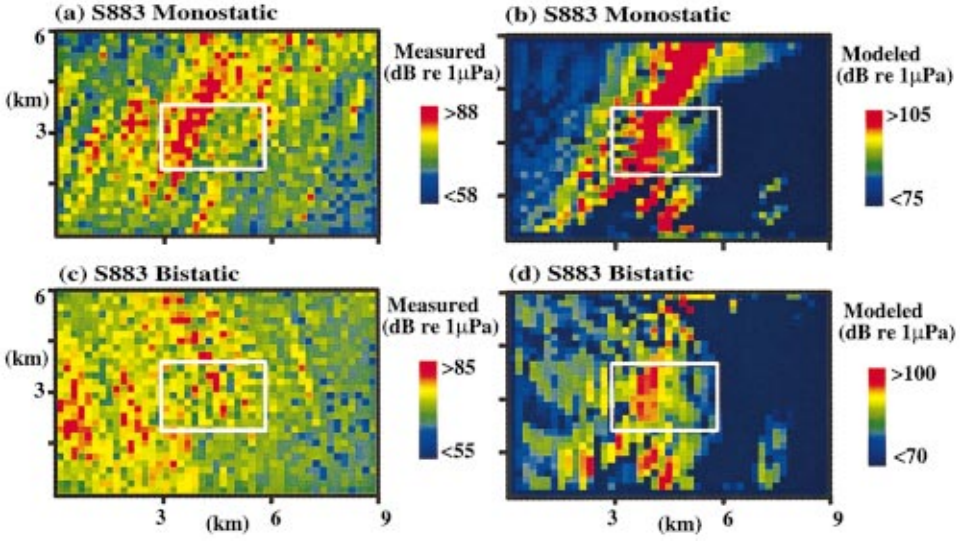


FIG. 20. Charts of the measured and modeled reverberation for S883 over the SW corner of C′ at 200-m resolution including the SW box. (a) Measured monostatic reverberation. (b) Modeled monostatic reverberation. (c) Measured bistatic reverberation. (d) Modeled bistatic reverberation.

plays a relatively constant behavior, except for $\Omega_r < -60°$, where the roll-off observed at these extreme azimuths is primarily due to the shadowing described in the mean TL curves. An average value of roughly $-13$ dB is obtained by averaging the mean strength of the scattering distribution across the entire $\pm 90°$ range of receiver azimuths. This constant value falls within all error bars.

## V. COMPARISON OF BIAZIMUTHAL SCATTERING DISTRIBUTIONS OVER B′ and C′

The biazimuthal scattering distributions as well as measured and modeled reverberation for the two geologically distinct B′ and C′ abyssal hills are compared in this section at 200-m resolution. First, the curves of the mean reverberation level measured across the C′ scarp and the two B′

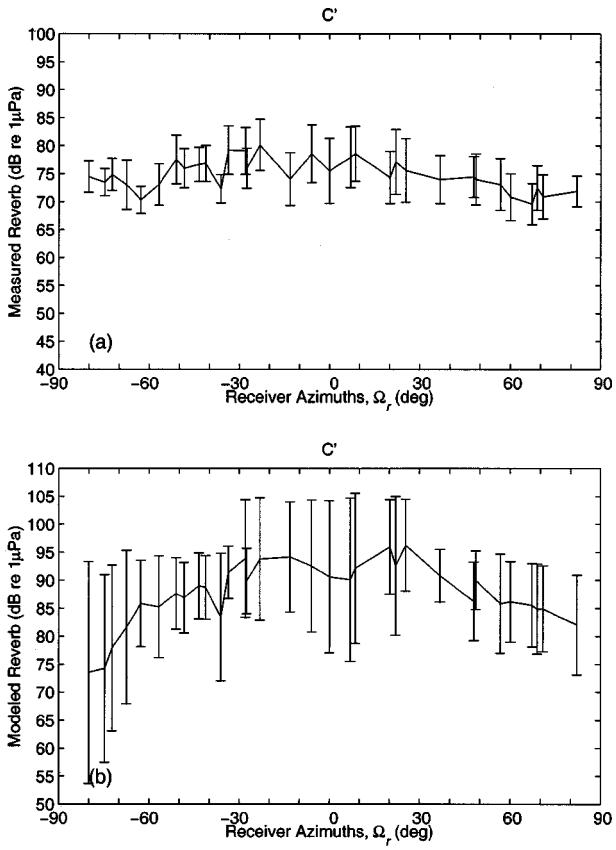


FIG. 21. (a) Mean measured reverberation level $\langle R(x,y|\Omega_i,\Omega_r)\rangle_{A_{C'}}$, and (b) mean modeled reverberation level $\langle R_M(x,y|\Omega_i,\Omega_r)\rangle_{A_{C'}}$ computed over the SW box of C′ as a function of receiver azimuth $\Omega_r$, along with their respective standard deviations, $\sigma_{A_{C'}}\{R(x,y)\}$ and $\sigma_{A_{C'}}\{R_M(x,y)\}$.

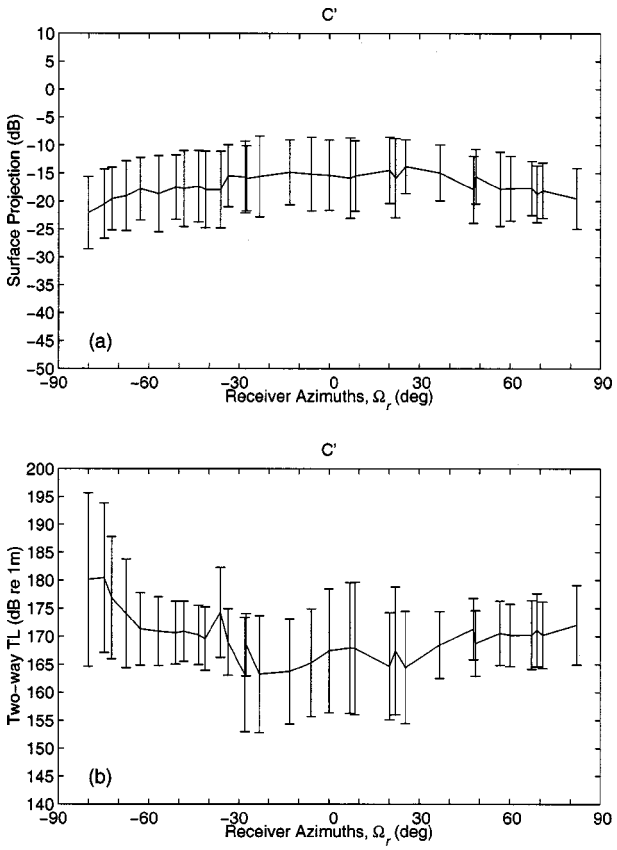


FIG. 22. (a) The mean surface projection $\langle C_i(x,y|\Omega_i,\Omega_r) + C_r(x,y|\Omega_i,\Omega_r)\rangle_{A_{C'}}$, and (b) the mean two-way transmission loss $\langle \mathrm{TL}_i(x,y|\Omega_i,\Omega_r) + \mathrm{TL}_r(x,y|\Omega_i,\Omega_r)\rangle_{A_{C'}}$, computed over the SW box of C′ as a function of receiver azimuth $\Omega_r$.

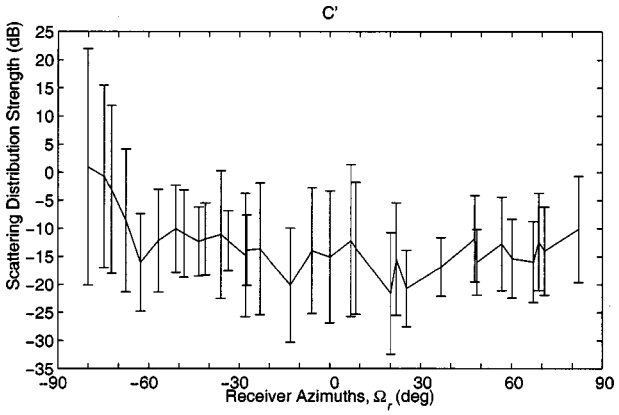


FIG. 23. The mean strength of the biazimuthal scattering distribution estimated over the SW box of $C'\langle\hat{\tilde{F}}(x,y|\Omega_i,\Omega_r)\rangle_{A_{C'}}$ as a function of receiver azimuth $\Omega_r$ along with its standard deviation $\sigma_{A_{C'}}\{\hat{\tilde{F}}(x,y)\}$.

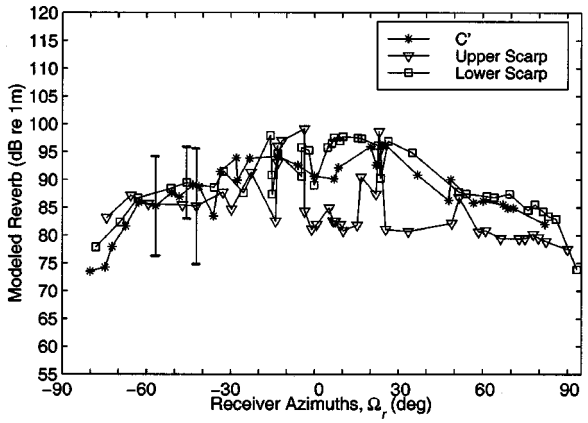


FIG. 25. Comparison of the mean reverberation levels, at 200-m resolution, modeled over the C′ scarp and the two B′ scarps as a function of receiver azimuth $\Omega_r$. Their typical standard deviations are plotted on each curve to illustrate the spread of modeled reverberation.

scarps are plotted as a function of receiver azimuth $\Omega_r$ in Fig. 24. A typical standard deviation is plotted on each curve to illustrate the spread of measured reverberation over these scarps. Generally, the mean values of all three curves are relatively uniform across the $\pm 90°$ receiver azimuths. Although the reverberation levels measured over the C′ scarp are occasionally 2–5 dB lower than those of the B′ scarps at some receiver azimuths, these differences lie within the roughly 6-dB standard deviation of all curves. As a result, one may conclude that there is no significant difference between the mean reverberation levels measured over the B′ and C′ scarps at $\frac{1}{2}$ CZ, and that at $\frac{1}{2}$ CZ reverberation measured over the major scarps of these two distinct abyssal hills is homogeneous across nonforward receiver azimuths.

Curves of the mean reverberation level modeled over the C′ scarp and the two B′ scarps, at 200-m resolution, are plotted as a function of receiver azimuth $\Omega_r$ in Fig. 25. While the B′ lower scarp and C′ SW scrap show regular convex behavior with peak values within $|\Omega_r|<30°$, the B′ upper scarp exhibits some fluctuations within $|\Omega_r|<30°$, which often exceed 10 dB. As discussed in Ref. 3, these fluctuations occur when the upper scarp falls into the shadow zone of the source main beam's refractive path. A similar shadowing effect is apparently revealed in the C′ curve for $\Omega_r<-60°$, where a 10-dB roll-off is observed. The modeled reverberation curves over the B′ lower scarp and C′ show a better match, for $\Omega_r>-60°$, since these two sites are well insonified by the source's main beam.

The strengths of the biazimuthal scattering distributions, estimated over the C′ scarp and the two B′ scarps, are plotted as a function of receiver azimuth $\Omega_r$ in Fig. 26. Large fluctuations for the B′ upper scarp are observed within $|\Omega_r|<30°$ due to shadowing. A constant line at roughly $-11$ dB can be drawn across the entire set of receiver azimuths for the C′ and B′ curves that still falls within all the error bars of roughly 10 dB and is centrally located when the means of all three curves are taken into account.

## VI. DISCUSSION AND CONCLUSIONS

The bistatic scattering characteristics of two geologically distinct abyssal hills located on the western flank of the Mid-Atlantic Ridge, composed of *outside corner* and *inside corner* crust and referred to as B′ and C′, respectively, are experimentally compared. The levels of bistatic reverberation, measured from scarps on the two abyssal hills in bi-

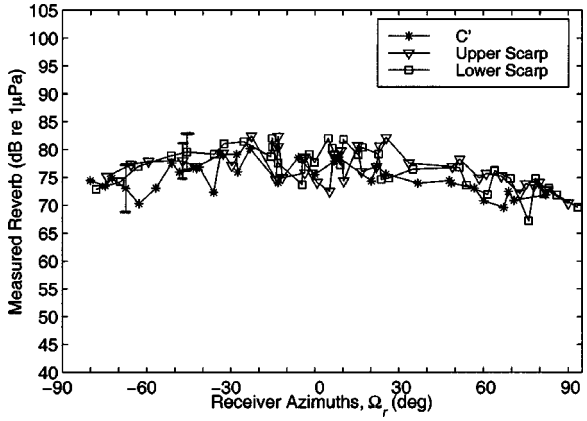


FIG. 24. Comparison of the mean reverberation levels, at 200-m resolution, measured over the C′ scarp and the two B′ scarps as a function of receiver azimuth $\Omega_r$. Their typical standard deviations are plotted on each curve to illustrate the spread of measured reverberation.

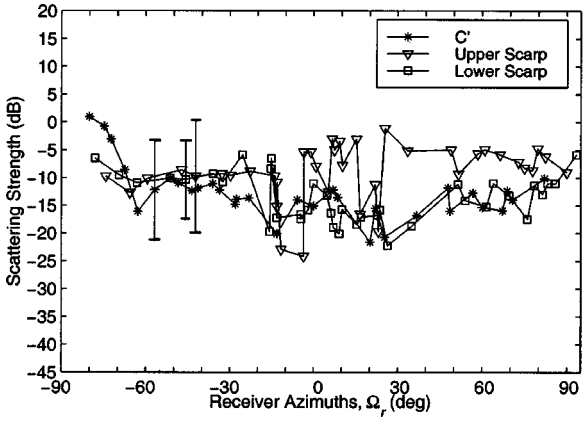


FIG. 26. Comparison of the mean biazimuthal scattering distribution strengths, at 200-m resolution, estimated over the C′ scarp and the two B′ scarps as a function of receiver azimuth $\Omega_r$. Their typical standard deviations are plotted on each curve to illustrate the spread of mean strengths.

static experiments from $\frac{1}{2}$ CZ stand-off, exhibit nearly identical, constant azimuthal dependencies. The mean biazimuthal scattering distributions of scarps on the two abyssal hills are also found to exhibit nearly identical and constant azimuthal dependencies with mean strength equal to $-11$ dB *when estimated from supporting bathymetry sampled at* 200-m *intervals*. Higher-resolution supporting bathymetry, only available at B′ and not at C′, sampled at 5-m intervals reveals that the projected area of the B′ scarps, as seen by refracted rays traveling from source to bistatic receiver at $\frac{1}{2}$ CZ, is significantly undersampled with the 200-m sampled bathymetry. This undersampling leads to a uniform bias of roughly $-6$ dB in the level of modeled bistatic reverbation from the B′ scarps and, consequently, a uniform bias of $+6$ dB in the strength of the mean biazimuthal scattering distributions of the B′ scarps. The strength of the mean biazimuthal scattering distributions of the B′ scarps is more accurately given by the constant $-17$ dB $\pm 8$ dB when estimated from the high-resolution bathymetry sampled at 5-m intervals. A general conclusion is that the use of bathymetry that undersamples the projected area of the seafloor within the resolution footprint of the towed-array system can lead to significant overestimates in the strength of seafloor scattering.

It is significant that although the introduction of 5-m sampled bathymetry revealed the B′ scarps to be comprised of a highly nonplanar network of canyons and gullies ($\sim$200-m scale) that is not resolved in the 200-m sampled bathymetry, the azimuthal dependence of the mean scattering distributions of the scarps remained constant when estimated with the two different bathymetric samplings and only differed by a constant 6-dB offset. The explanation is related to the fact that the sonar system resolution footprint, with cross range extent of roughly 1 km at $\frac{1}{2}$ CZ, typically averages over many canyons and gullies and that the mean biazimuthal scattering distribution averages over a large number of footprints on a given scarp. Delicate, coherent directional differences in scattering due to small-scale structures, such as canyons and gullies, then average out while the overall expected level is still sensitive to the mean projected area within a given resolution footprint since, even on average, this is a first-order quantity directly proportional to the total flux received from the patch.

We expect the same argument to apply to scattering from the C′ scarp, and so hypothesize that the mean biazimuthal scattering distribution will still have constant strength, but will be reduced by a fixed positive offset if the 200-m sampled bathymetry at C′ underestimates the projected area of seafloor sites within the system resolution footprint. Our expectation is that the 200-m sampled bathymetry does indeed underestimate these projected areas.

We then conclude that long-range reverberation from prominent geological features of the Mid-Atlantic Ridge, and likely other midocean ridges, can be adequately modeled as having Lambertian scattering characteristics. We hypothesize that the albedo of $\pi/10^{1.7}$, measured for the two major scarps on the B′ abyssal hill with a more than adequate bathymetric sampling density, provides a reasonable estimate of the albedo of all abyssal hills comprised of *outside corner* crust and may also provide a good estimate of the albedo of abyssal hills comprised of *inside corner* crust. We take the albedo of $\pi/10^{1.1}$, measured for an abyssal hill comprised of *inside corner* crust from potentially undersampled bathymetry, as an upper bound on albedos of abyssal hills comprised of *inside corner* crust.

## APPENDIX

This Appendix provides the equations used for modeling reverberation and estimating the mean biazimuthal scattering distribution strength. Derivations of these equations are given in Sec. 2C of Ref. 3. The resolution footprint, at $\frac{1}{2}$ CZ of 33-km range, occupies an annular sector with dimensions of roughly 50 by 1000 m that are large compared to the mean acoustic wavelength of 6.7 m. The total received field from the sonar footprint can therefore be treated as stochastic and diffuse. The expected intensity radiated from the resolution patch can be charted to the center of that patch by performing the convolution

$$\langle I(x,y)|r_i,r_r)\rangle \approx \int\int_{A_f(x,y|r_i,r_r)} f(\theta_i,\phi_i;\theta_r,\phi_r) w l_i l_r \cos\theta_i \cos\theta_r \, dX\, dY, \tag{A1}$$

where $\theta$ and $\phi$ denote the elevation and azimuth angles with respect to the seafloor's surface at $(X,Y)$, and the subscripts $i$ and $r$ indicates the incident and scattered angles, respectively. The function $f$ is known as the bidirectional scattering distribution function (BSDF) of the surface, which is similar to the concept of bidirectional reflectance distribution function in the modern radiometry.[3,15] Note that the traditional scattering strength in underwater acoustics corresponds to $S=f\cos\theta_i,\cos\theta_r$. When $f$ is an angle-independent constant, it is related to the surface albedo $\alpha$ by $f=\alpha/\pi$, and becomes equivalent to the coefficient $\mu$ commonly used in the seafloor scattering-strength estimation. The other factors in Eq. (A1) include the transmission power $w$, and the transmission factors $l_i$ and $l_r$. This result can be expressed in decibels as

$$R_{\langle I\rangle}(x,y|r_i,r_r) \approx W + 10\log\left(\int\int_{A_f(x,y|r_i,r_r)} 10^{[F(\theta_i,\phi_i;\theta_r,\phi_r)-\mathrm{TL}_i-\mathrm{TL}_r+C_i+C_r]/10} dX\, dY\right), \tag{A2}$$

with the following set of notations: $R_{\langle I\rangle}$: Reverberation level in dB $re$ 1 $\mu$Pa, $F$: Biazimuthal scattering distribution's strength in dB $re$ 1 $\mu$Pa@1 m, $F=10\log f$, $W$: Source level in dB $re$ 1 $\mu$Pa@1 m, $W=10\log w$, $\mathrm{TL}_i$: Transmission loss from source to scattering patch in dB $re$ 1 m, $\mathrm{TL}_i=10\log l_i$, $\mathrm{TL}_r$: Transmission loss from the scattering patch to the receiver in dB $re$ 1 m, $\mathrm{TL}_r=10\log l_r, C_i$: Surface projection in the direction of incident refracted wave in dB, $C_i=10\log(\cos\theta_i)$, $C_r$: Surface projection in the direction of scattered refracted wave in dB, $C_r=10\log(\cos\theta_r)$, $A_f$: Sonar resolution footprint area in square meters.

Modeled reverberation is from elemental seafloor patches with $F=0$ that scatter equally in all directions so that

$$R_M(x,y|r_i,r_r) = W+10\log\left(\int\int_{A_f(x,y|r_i,r_r)} 10^{[-\mathrm{TL}_i-\mathrm{TL}_r+C_i+C_r]/10}\,dX\,dY\right). \tag{A3}$$

This leads to a simple linear equation for the mean strength of the scattering distribution over the resolution footprint

$$\overline{F}(x,y|r_i,r_r)=R_{\langle I\rangle}(x,y|r_i r_r)-R_M(x,y|r_i,r_r), \tag{A4}$$

where the dependence on the incident and scattered angles is integrated over the resolution footprint. Finally, the maximum likelihood estimate for $\overline{F}$ is given by

$$\hat{\overline{F}}(x,y|r_i,r_r)=R(x,y|r_i,r_r)-R_M(x,y|r_i,r_r), \tag{A5}$$

which is the difference between reverberation measured with MAE data and modeled with $F=0$.


[1] Acoustic Reverberation Special Research Program, Initial Report, edited by J. Orcutt, Scripps Institution of Oceanography (1993).
[2] N. C. Makris, ''Proposed experiment,'' in Acoustic Reverberation Special Research Program Research Symposium, Woods Hole Oceanographic Institution (1992).
[3] N. C. Makris, C. S. Chia, and L. T. Fialkowski, ''The bi-azimuthal scattering distribution of an abyssal hill,'' J. Acoust. Soc. Am. **106**, 2491–2512 (1999).
[4] N. C. Makris, L. Avelino, and R. Menis, ''Deterministic reverberation from ocean ridges,'' J. Acoust. Soc. Am. **97**, 3547–3574 (1995).
[5] B. E. Tucholke and J. Lin, ''A geological model for the structure of ridge segments in slow spreading ocean crust,'' J. Geophys. Res. **99**, 11937–11958 (1994).
[6] N. C. Makris, ''The effect of saturated transmission scintillation on ocean acoustic intensity measurements,'' J. Acoust. Soc. Am. **100**, 769–783 (1996).
[7] B. E. Tucholke, J. Lin, M. C. Kleinrock, M. A. Tivey, T. B. Reed, J. Goff, and G. E. Jaroslow, ''Segmentation and crustal structure of the western Mid-Atlantic Ridge flank, 25°25′–27° 10′N and 0–29 m.y.,'' J. Geophys. Res. **102**, 10203–10223 (1997).
[8] K. B. Smith, W. S. Hodgkiss, and F. D. Tappert, ''Propagation and analytic issues in the prediction of long-range reverberation,'' J. Acoust. Soc. Am. **99**, 1387–1404 (1996).
[9] A. J. Harding, M. A. H. Hedlin, and J. A. Orcutt, ''Migration of backscatter data from the Mid-Atlantic Ridge,'' J. Acoust. Soc. Am. **103**, 1787–1803 (1998).
[10] C. S. Chia, ''A Comparison of Bistatic Scattering from Two Geologically Distinct Mid-Ocean Ridges,'' S. M. thesis, MIT, Cambridge, MA, 1999.
[11] N. C. Makris and B. Gardner, ''Planned tracks/waypoints, runs 3–9,'' in Acoustics Reverberation Special Research Program Main Acoustics Experiment, Initial Report, Scripps Institution of Oceanography (1993), pp. 65–80.
[12] J. R. Preston, E. Michelozzi, L. Troiano, and R. Hollett, *Cruise Report on RV ALLIANCE cruise MARE 5 July–1 August 1993 SACLANTCEN's Joint Experiment with ONR's ARSRP Group*, Report M-112 (SACLANT Undersea Research Centre, LaSpezia, Italy, 1993).
[13] N. C. Makris and J. M. Berkson, ''Long-range backscatter from the Mid-Atlantic Ridge,'' J. Acoust. Soc. Am. **95**, 1865–1881 (1994).
[14] N. C. Makris, ''Imaging ocean-basin reverberation via inversion,'' J. Acoust. Soc. Am. **94**, 983–993 (1993).
[15] B. K. P. Horn and R. W. Sjoberg, ''Calculating the reflectance map,'' Appl. Opt. **18** (No. 11), 1770–1779 (1979).